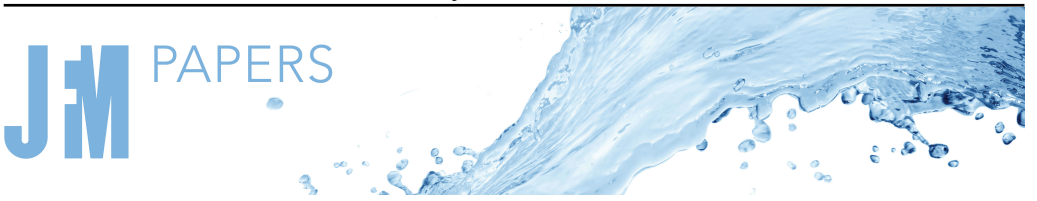
J. Fluid Mech. (2026), *vol.* 1031, A1, doi:10.1017/jfm.2026.11280



Nonlinear optimal forcing analysis on subsonic flow around an airfoil

Nobutaka Taniguchi[1,2], **Yuya Ohmichi**[3] and **Kojiro Suzuki**[4]

[1]Department of Aeronautics and Astronautics, The University of Tokyo, Japan

[2]Institute of Fluid Science, Tohoku University, Japan

[3]Aeronautical Technology Directorate, Japan Aerospace Exploration Agency, Japan

[4]Department of Advance Energy, The University of Tokyo, Graduate School of Frontier Sciences, Japan

Corresponding author: Nobutaka Taniguchi, nobutaka.taniguchi.c1@tohoku.ac.jp

(Received 7 August 2025; revised 11 December 2025; accepted 30 January 2026)

Active flow control often exploits disturbance amplification mechanisms to achieve desired flow properties. Recently, theoretical predictions of optimal control based on stability analysis have gained traction. However, these methods are limited in their ability to predict nonlinear control strategies, such as burst-mode actuation for separated flows, which involve intermittent and high-amplitude forcing. To address this limitation, we developed a nonlinear optimal forcing analysis based on optimal perturbation theory. This method is specifically designed to capture non-harmonic forcing patterns and the nonlinear temporal evolution of the disturbance field. We applied this method to the two-dimensional high-subsonic, low-Reynolds number flow around a NACA0012 airfoil to reattach the separated flow and investigate the onset mechanism of low-frequency oscillation. The analysis identified an optimal temporal forcing pattern characterized by damped oscillation. This forcing exploits flow amplification mechanisms over the separation bubbles, promoting the formation of spanwise vortices in the shear layer. When implemented as a periodic forcing concentrated at the separated point, these vortices were stably generated, resulting in a significant lift increase via momentum exchange. A key finding is that the application of this optimal forcing induced long-term changes in the flow field, driven by the transient emergence of low-frequency oscillations. Furthermore, we explored the intermittent application of this forcing and found that an appropriate duty cycle can enhance the lift coefficient while reducing energy consumption.

Key words: separated flows, instability control, shear-flow instability

© The Author(s), 2026. Published by Cambridge University Press. This is an Open Access article, distributed under the terms of the Creative Commons Attribution licence (https://creativecommons.org/licenses/by/4.0/), which permits unrestricted re-use, distribution and reproduction, provided the original article is properly cited.

https://doi.org/10.1017/jfm.2026.11280 Published online by Cambridge University Press

1. Introduction

The optimal design of flow control is a key application of stability analysis. Stability analysis provides a theoretical framework for predicting the evolution of perturbations superimposed on a basic flow. In flow control application, understanding the receptivity to small perturbations and the amplification of specific disturbances offers important insights to construct the flow control strategy to achieve desirable flow properties. For instance, sensitivity analysis studies (Giannetti & Luchini 2007) have demonstrated that appropriately designed control can lower the receptivity of the flow past a cylinder to perturbations (Marquet, Sipp & Jacquin 2008; Del Guercio, Cossu & Pujals 2014), thereby reducing the linear instability of the base flow field. In contrast, active flow control exploits amplification mechanism of the base flow field, resulting in small amplitude of forcing to change the flow field. In the literature, the amplification mechanisms have been utilized to control the separated flow over an airfoil (Yeh & Taira 2019; Gross, Marks & Sondergaard 2024) and tonal noise in cavity flows (Liu *et al.* 2021). Because these theoretical predictions of flow control reduce the cost of experiments and high-accuracy numerical calculations, the application of stability analysis to flow control is expected to increase its importance in fluid dynamics.

The amplification of the disturbance field results from the non-normality of the linearized Navier–Stokes (N–S) equations and the nonlinear time-evolution of the disturbance field. The non-orthogonality of the eigenvectors of the linearized N–S equations is known to result in the amplification of the linear disturbance field. In other words, the superposition of linearly stable eigenvectors may induce transient growth during finite-time evolution (Farrell 1988; Gustavsson 1991; Butler & Farrell 1992; Reddy & Henningson 1993). When considering external forces, resolvent analysis is formulated to evaluate the amplification at a specific frequency (Trefethen *et al.* 1993; Jovanović & Bamieh 2005). This transient amplification of the disturbance field is attributed to the pseudospectra of the linear operator of the N–S equation, as described by Trefethen *et al.* (1993). These analyses are currently classified within a framework of input–output analysis that reveals flow properties based on the initial disturbance fields and the harmonic forcing as inputs (Schmid 2007).

Generalized input–output analysis has been proposed based on the computational performance enhancement stemming from these pioneering studies, including the consideration of a global disturbance field (Monokrousos *et al.* 2010) and nonlinear disturbance evolution (Pringle & Kerswell 2010; Cherubini *et al.* 2011; Huang & Hack 2020). An important consequence of nonlinear nonmodal analysis is the existence of disturbance amplification supported by the nonlinear interactions of the finite-amplitude disturbances, which resulted in the important concept of the minimal seed that induces the laminar–turbulent transition with minimal input energy (Cherubini *et al.* 2011; Pringle, Willis & Kerswell 2012). In external flow control applications, the importance of considering the finite amplitude of forcing lies in the modification of the optimal forcing distribution with increasing amplitude (Laroussi, Djebbi & Moussa 2014; Taniguchi *et al.* 2024*b*). Many applications of these analyses have been reported including incompressible boundary layers (Monokrousos *et al.* 2010; Cherubini *et al.* 2011) and incompressible and compressible pipe flows (Pringle & Kerswell 2010; Huang & Hack 2020).

As reviewed by Greenblatt & Wygnanski (2000), the amplification mechanism in shear flow plays a critical role in active separation control. In experiments, it is well known that the acoustic excitation reduces the flow separations (Zaman 1992). Recently, burst-mode actuation of dielectric barrier discharge (DBD) plasma actuator (Greenblatt *et al.* 2008;

https://doi.org/10.1017/jfm.2026.11280 Published online by Cambridge University Press

Kotsonis & Veldhuis 2010; Asada *et al.* 2015; Sekimoto, Nonomura & Fujii 2017) has been proposed for flow control applications. The characteristic of burst mode actuation is that one cycle of flow control involves an actuation duration and a quiescent period, allowing the evolution of the disturbance field to be promoted by flow nonlinearity. In large-eddy simulations of burst-mode actuation using a DBD plasma actuator on separated flow around an airfoil, Asada *et al.* (2015) reported that two-dimensional spanwise vortices evolved into coherent structures, leading to an increase in lift by promoting flow reattachment.

As noted previously, since the burst mode actuation is composed of actuation and quiescent phases within one cycle, it is difficult to treat it under the assumption of single harmonic forcing (Trefethen *et al.* 1993). Applying stability analysis to active flow control, especially with burst-mode actuation of a DBD plasma actuator, thus requires considering non-harmonic external forcing with nonlinear time-evolution. It is worth noting that nonlinear resolvent analysis using the harmonically balanced N–S equations has been recently proposed by Rigas, Sipp & Colonius (2021). However, because a large number of harmonic waves are needed to represent the forcing pattern of burst-mode actuation, we chose to extend the nonlinear optimal perturbation analysis (Pringle & Kerswell 2010; Cherubini *et al.* 2011; Huang & Hack 2020) to external forcing with temporal excitation patterns. Because the original analysis method was designed to analyse the nonlinear time-evolution of disturbance field by directly solving the N–S equations, it has no theoretical restrictions regarding the magnitude of the disturbance field and steadiness of the base flow field.

In this study, we focus on optimizing non-harmonic, high-intensity forcing to reattach separated flow. While flow separation typically triggers an immediate laminar-to-turbulent transition, the flow remains predominantly laminar in the low Reynolds number regime (typically chord-based Reynolds number $Re < 10^5$). This separation induces strong nonlinearities, characterized by a negative slope of the lift coefficient (Ohtake, Nakae & Motohashi 2007; Winslow *et al.* 2018) and low-frequency oscillations (Bouhadji & Braza 2003; Jones, Sandberg & Sandham 2006; Moise, Zauner & Sandham 2024). Bouhadji & Braza (2003) investigated the two-dimensional unsteady motion around a zero-incidence NACA0012 airfoil at Mach number $0.5 \leqslant M < 1.0$ and $Re = 10\,000$. They reported that alternating boundary layer separation on the upper and lower surfaces drives the oscillation. Such high-subsonic, low-Reynolds-number flows have gained significant attention due to the ongoing development of aircraft for the Martian environment (Takagaki *et al.* 2008; Nagata *et al.* 2020; Koning *et al.* 2024). Given the strict weight constraints in these applications, plasma actuators present a promising control strategy. Furthermore, Moise *et al.* (2024) highlighted the link between low-frequency oscillations at low Reynolds numbers and the buffet phenomenon at higher Reynolds numbers. Therefore, it is essential to elucidate the onset mechanism of these low-frequency oscillations and, concurrently, investigate control methods for flow reattachment in this specific regime.

This study seeks to identify the optimal external forcing required to reattach separated flow regions, leveraging optimal disturbance analysis. Since this problem is closely related to existing research based on optimization, we present a focused review of relevant references. Early efforts in flow control optimization utilized adjoint methods to obtain the optimal distribution of steady suction to suppress linear disturbance growth (Pralits, Hanifi & Henningson 2002; Pralits & Hanifi 2003). These foundational studies paved the way for various optimization approaches, including singular value decomposition techniques for identifying optimal controller locations (Lim & Kim 2004), and methods for optimizing actuator distribution (Mao, Blackburn & Sherwin 2015; Natarajan, Freund &

https://doi.org/10.1017/jfm.2026.11280 Published online by Cambridge University Press

Bodony 2016) or developing feed-forward strategies (Juillet, McKeon & Schmid 2014). More recently, the application of optimization has expanded to address highly nonlinear flow phenomena, with diverse objectives such as maximizing heat transfer in pipe flow (Chu, Marensi & Willis 2025) and minimizing drag in turbulent flow fields using machine learning (Vinuesa *et al.* 2022; Suárez *et al.* 2025). Our approach builds upon the adjoint optimization framework with a focus on achieving the highly nonlinear objective of reattaching massive separated flow regions.

This study identifies the optimal external force to reattach such detached regions based on optimal disturbance analysis. Since this problem setting is closely related to previous fluid control researches based on optimization problems, we present a review of the references. Pralits *et al.* (2002) and Pralits & Hanifi (2003) obtained the optimal distribution of steady suction to control the disturbance growth, based on the adjoint optimization of the forcing. To suppress the disturbance growth of flow field, many studies have been conducted including singular value decomposition technics (Lim & Kim 2004), actuator distribution (Mao *et al.* 2015; Natarajan *et al.* 2016) and feed-forward control strategy (Juillet *et al.* 2014). More recently, Chu *et al.* (2025) obtained the optimal forcing to maximize the heat transfer in pipe flow. Moreover, a machine learning approach is also attempted to solve the optimization problem to reduce the drag in a turbulent flow field (Vinuesa *et al.* 2022; Suárez *et al.* 2025).

The ultimate goal of this research is to develop a control method that considers nonlinearity to control and reattach separated flow. To achieve this, the objectives of this research are divided into two stages. In the first stage, we identify the optimal external force applied near the wall surface to reattach the separated base flow. Second, we demonstrate the application of optimal forcing to increase the lift coefficient leveraging the properties of the optimal forcing. The paper is organized as follows. In § 2, we present the formulation of our nonlinear optimal forcing (NLOF) analysis, and § 2.5 describes the characteristics of the base flow relevant to applying the analysis. Section 3 details the characteristics of the NLOF analysis solution, and we discuss the origin of the low-frequency oscillation by analysing the transient flow changes induced by optimal forcing using modal analysis. Finally, in § 4, we discuss the application of impulsive optimal forcing analysis to increase the lift coefficient.

2. Nonlinear optimal forcing analysis

2.1. *Governing equations*

In this study, we consider the non-dimensional compressible N–S equations with external forces as the governing equations. The equation is non-dimensionalized using the velocity, density and temperature of free stream flow and chord length of NACA0012 airfoil. The compressible N–S equations consist of the equations of mass, momentum and pressure as

$$\frac{\partial \rho}{\partial t} = -\frac{\partial}{\partial x_j}(\rho u_j), \tag{2.1}$$

$$\frac{\partial \rho u_i}{\partial t} = -\frac{\partial}{\partial x_j}(\rho u_i u_j) - \frac{\partial p}{\partial x_i} + \frac{\partial \tau_{ij}}{\partial x_j} + \rho h_i, \tag{2.2}$$

$$\frac{\partial p}{\partial t} = -\frac{\partial}{\partial x_j}(p u_j) - (\gamma - 1)\left\{ p\frac{\partial u_j}{\partial x_j} - \tau_{ij}\frac{\partial u_i}{\partial x_j} - \frac{\partial \mathcal{Q}_j}{\partial x_j} \right\}, \tag{2.3}$$

where ρ, u_x, u_y, p, γ represent the density, velocity in x-direction, velocity in y-direction, pressure and specific heat ratio, respectively. Here, h_x, h_y are the external forces, and the

https://doi.org/10.1017/jfm.2026.11280 Published online by Cambridge University Press

viscous stress tensor τ_{ij} and heat flux $\mathcal{Q}_i$ are expressed as

$$\tau_{ij} = \frac{\mu}{Re}\left(\frac{\partial u_i}{\partial x_j} + \frac{\partial u_j}{\partial x_i} - \frac{2}{3}\delta_{ij}\frac{\partial u_k}{\partial x_k}\right), \tag{2.4}$$

and

$$\mathcal{Q}_i = \frac{\kappa}{(\gamma-1)M^2RePr}\frac{\partial \Theta}{\partial x_i}, \tag{2.5}$$

where M, Re, Pr are the Mach number, Reynolds number and Prandtl number, respectively. In this study, we fixed $Pr = 0.7$ and $\gamma = 1.4$ for the air flow around an airfoil. In the above equation, Θ represents the temperature, and the state equation is given by

$$p = \frac{\rho\Theta}{\gamma M^2}. \tag{2.6}$$

For the coefficients of viscosity μ and thermal conductivity κ. For the viscosity, we applied Sutherland law of viscosity as

$$\mu^* = 1.458 \times 10^{-5}\frac{\Theta^{*3/2}}{\Theta^* + 110.4}, \quad \Theta^* \geqslant 110.4\,\mathrm{K} \tag{2.7}$$

where Θ^*[K] is the dimensional temperature. We assumed the free stream temperature was 273.15K for all the computation conditions.

2.2. *Problem settings*

2.2.1. *Definition of base flow and external forcing*

In this section, we define the problem setting of our optimal forcing analysis. We consider a solution trajectory of the governing equation of compressible N–S equations as the base flow, $\boldsymbol{Q}(t, \boldsymbol{x})$, over a range of $0 \leqslant t \leqslant t_f$, where t_f is a given evaluation time. Here, $\boldsymbol{Q}$ is the state vector of the flow field, specifically $\boldsymbol{Q} = (\bar{\rho}, \bar{\rho}\bar{u}_x, \bar{\rho}\bar{u}_y, \bar{p})^T$ where $\bar{\rho}, \bar{u}_x.\bar{u}_y, \bar{p}$ are the density, x-velocity, y-velocity and pressure of the base flow, respectively. We assume that the base flow $\boldsymbol{Q}(t, \boldsymbol{x})$ is dependent on both time and space, as the assumption of a steady base flow is not required in the subsequent discussion.

We consider the application of external forcing, $\boldsymbol{h}(t, \boldsymbol{x})$, to the flow field, assuming that the flow changes from $\boldsymbol{Q}(t, \boldsymbol{x})$ to $\boldsymbol{q}(t, \boldsymbol{x})$ due to the forcing. We define the disturbance flow field as $\boldsymbol{q}'(t, \boldsymbol{x}) = \boldsymbol{q}(t, \boldsymbol{x}) - \boldsymbol{Q}(t, \boldsymbol{x})$. Here, $\boldsymbol{q}(t, \boldsymbol{x})$ represents the flow field perturbed by the external forces. For these external forces, we consider $\boldsymbol{h} = (0, h_x, h_y, 0)^T$ where h_x and h_y are the body forces in the x- and y-directions, respectively. Based on the above descriptions, the perturbed flow field $\boldsymbol{q}(t, \boldsymbol{x})$ satisfies the compressible N–S equations with external forces as

$$\partial_t \boldsymbol{q}(t, \boldsymbol{x}) = \mathcal{F}[\boldsymbol{q}(t, \boldsymbol{x})] + \rho\boldsymbol{h}(t, \boldsymbol{x}), \tag{2.8}$$

where $\mathcal{F}$ formally represents the right-hand side of the compressible N–S equations. Furthermore, we assume the separation of variables in the external forces as

$$\boldsymbol{h}(t, \boldsymbol{x}) = f(t)\boldsymbol{g}(\boldsymbol{x}), \tag{2.9}$$

where $f(t)$ is a scalar function representing the temporal distribution and $\boldsymbol{g}(\boldsymbol{x})$ is a vector function representing the spatial distribution. In flow control applications, this assumption is considered natural because the separation of variables into spatial and temporal distributions corresponds to fixing the location of control devices while modulating their actuation over time.

https://doi.org/10.1017/jfm.2026.11280 Published online by Cambridge University Press

2.2.2. *Variational formulation*

In this setting, we define the problem as determining the optimal forcing field that changes the base flow under appropriate constraint conditions. We introduce an evaluation function, $\mathcal{G}[t_f, \boldsymbol{q}, \boldsymbol{Q}]$ to quantify these flow field changes. For selecting the evaluation function, several approaches have been proposed. These include the incompressible disturbance energy (Huang & Hack 2020), compressible extensions of disturbance energy (Hanifi, Schmid & Henningson 1996) and the time-average of total entropy production (Monokrousos *et al.* 2011; Duguet *et al.* 2013; Taniguchi *et al.* 2024*a*). Specifically, Taniguchi *et al.* (2024*a*) discussed the differences in nonlinear optimal perturbation fields for subsonic flow around a NACA0012 airfoil when using the first and third metrics. They showed that the latter exhibits high sensitivity to changes related to wall friction. We define the evaluation function as the time-averaged entropy production, defined as

$$\mathcal{G}[t_f, \boldsymbol{q}(t, \boldsymbol{x});\ \boldsymbol{Q}(t, \boldsymbol{x})] = \int_0^{t_f} P[\boldsymbol{q}(t, \boldsymbol{x})]\mathrm{d}t, \tag{2.10}$$

and $P[\boldsymbol{q}(t, \boldsymbol{x})]$ is the integral of the entropy production of the instantaneous flow field over the entire computational domain, Ω. This term is given by

$$P[\boldsymbol{q}(t, \boldsymbol{x})] = \int_\Omega \frac{\kappa}{\Theta^2}|\nabla\Theta|^2 + \frac{\mu}{2\Theta}S : S - \frac{2}{3}\frac{\mu}{\Theta}\left(\frac{\partial u_j}{\partial x_j}\right)^2 \mathrm{d}V, \tag{2.11}$$

with

$$S_{ij} = \frac{\partial u_i}{\partial x_j} + \frac{\partial u_j}{\partial x_i}, \tag{2.12}$$

where μ and κ are the coefficients of viscosity and thermal conductivity, respectively. In this study, we employed the evaluation function in (2.10) because it provides a globally defined measure that is closely correlated with the recovery of wall friction, thereby serving as a promising indicator of flow reattachment.

As a constraint condition, we consider a constant energy input for the external forcing. To determine its spatial distribution, we extended the approach of nonlinear optimal perturbation analysis by Pringle & Kerswell (2010), Cherubini *et al.* (2011) and Huang & Hack (2020) to external forces. We define the constraints for optimal forcing as

$$E[\boldsymbol{g};\ \boldsymbol{Q}] := \int_\Omega \frac{1}{2}(g_x^2 + g_y^2)\mathrm{d}V = \delta_0^2, \tag{2.13}$$

where δ_0 is the given magnitude of the external forces. Without loss of generality, we can assume the L^2 norm of the temporal distribution is unity, given by

$$||f(t)||_2^2 = 1. \tag{2.14}$$

In this study, we use the variational formulation of optimal forcing analysis based on the nonlinear optimal perturbation method (Pringle & Kerswell 2010; Cherubini & De Palma 2013). In this formulation, we introduce the Lagrangian functional

$$\begin{aligned}\mathcal{L} = {} & \mathcal{G}[t_f; \boldsymbol{q}(t, \boldsymbol{x});\ \boldsymbol{Q}(t, \boldsymbol{x})] - \chi(||f(t)||_2^2 - 1) - \mu(E[\boldsymbol{g}(\boldsymbol{x});\ \boldsymbol{Q}(t_0, \boldsymbol{x})] - \delta_0^2) \\ & - \int_{t_0}^{t_f} \boldsymbol{\lambda}^*(t, \boldsymbol{x})\left\{\partial_t \boldsymbol{q}(t, \boldsymbol{x}) - \mathcal{F}[\boldsymbol{q}(t, \boldsymbol{x})] - \rho f(t)\boldsymbol{g}(\boldsymbol{x})\right\}\mathrm{d}t\end{aligned} \tag{2.15}$$

where μ, χ and $\boldsymbol{\lambda} = \boldsymbol{\lambda}(t, \boldsymbol{x})$ are the Lagrange multipliers.

https://doi.org/10.1017/jfm.2026.11280 Published online by Cambridge University Press

2.2.3. *Spatial distribution of forcing*

In this study, we use a DBD plasma actuator as the flow control device. Physically, a DBD plasma actuator consists of two thin electrodes mounted on the surface and a high-voltage power supply. Flow is induced by the plasma discharge between the two electrodes (Post & Corke 2004; Jukes *et al.* 2006). Given this set-up, it is reasonable to assume that the installation location of the plasma actuator can be freely determined. The wall-normal distribution, determined by the plasma's extension from the electrodes, typically exhibits a Gaussian-like profile (see figure 10 in Post & Corke (2004) for PIV measurements of the actual flow induced by a DBD actuator). Thus, modelling the DBD plasma actuator as a body force with separated wall-tangential and wall-normal distributions is a reasonable approach. However, a potential drawback of this formulation is that it permits the external forcing to be distributed over the entire airfoil surface, creating an unphysical scenario for a localized actuator. Consequently, we will revisit this issue in § 4, specifically discussing the applicability of extracting and applying the forcing only in locally concentrated regions to ensure a physically realizable control strategy.

Based on the above discussion, we further assume a separation of variables in the spatial distribution of forcing, $\boldsymbol{g}(\boldsymbol{x})$. For the wall-tangential direction ξ and wall-normal direction η, we assume that

$$\boldsymbol{g}(\boldsymbol{x}) = g_\eta(\eta)\boldsymbol{g}_\xi(\boldsymbol{x}), \tag{2.16}$$

where $\boldsymbol{g}_\xi(\boldsymbol{x})$ is the ξ-directional vector function, and $g_\eta(\eta)$ is the η-directional scalar function. Under this assumption, we consider $\boldsymbol{g}_\xi(\boldsymbol{x})$ as the target function for optimization, while $g_\eta(\eta)$ is a function determined by the source of external forcing. In the optimization, we do not impose any further assumptions on the wall-tangential distribution of the optimal forcing to ensure the flexibility of the optimization results.

For wall-normal distribution, we model the external force source as a plasma actuator (Post & Corke 2004), where the assumption in (2.16) is a much simpler model compared with the previous studies (Asada *et al.* 2015). This simplified assumption is incorporated to facilitate the optimization of the forcing, whereas rather detailed analysis would be required for practical application in control systems. For $g_{\boldsymbol{x}}(\eta)$, we adopt a Gaussian distribution, with a modification to enforce the boundary condition $\boldsymbol{h}(\boldsymbol{x}) = 0$ at $\eta = 0$ as

$$g_\eta(\eta) = \frac{\eta}{\sqrt{2\pi\sigma^2}} \exp\left(-\frac{(\eta-\mu)^2}{2\sigma^2}\right), \tag{2.17}$$

where σ and μ are constant free parameters that should be determined to suit the targeted control device. In this study, we used the values $\sigma = 0.001$ and $\mu = 0.005$ to align the forcing distribution with the height of the laminar separation bubble in the base flow.

2.2.4. *Euler–Lagrange equation*

To solve the maximization problem of the Lagrangian in (2.15), we derive the Euler–Lagrange equations. Taking the first variation of (2.15) yields

$$\frac{\partial \mathcal{L}}{\partial \boldsymbol{q}(t_f)} = 0 \Rightarrow \boldsymbol{\lambda}(t_f) = 0, \tag{2.18}$$

$$\frac{\partial \mathcal{L}}{\partial \boldsymbol{g}_\xi} = 0 \Rightarrow -\mu \int g_\eta^2 \mathrm{d}\eta \boldsymbol{g}_\xi + \int_0^{t_f} f(t) \int \rho \boldsymbol{\lambda} g_\eta \mathrm{d}\eta \mathrm{d}t = 0, \tag{2.19}$$

$$\frac{\partial \mathcal{L}}{\partial \boldsymbol{q}(t)} = 0 \Rightarrow \partial_t \boldsymbol{\lambda}(t) + \left(\frac{\partial \left(\mathcal{F}[\boldsymbol{q}(t)] + \rho(t) f(t) \boldsymbol{g}(t)\right)}{\partial \boldsymbol{q}(t)}\right)^\dagger \boldsymbol{\lambda}(t) = \left(\frac{\partial P[\boldsymbol{q}(t)]}{\partial \boldsymbol{q}(t)}\right)^\dagger, \tag{2.20}$$

https://doi.org/10.1017/jfm.2026.11280 Published online by Cambridge University Press

Algorithm 1 Optimization process of NLOF analysis

Input: initial guess of NLOF $\hat{q}_0^{(0)}$ given as a uniformly random field. Set ϵ_{spa}, ϵ_{tem} for the tolerance of updating residuals.
Output: estimated NLOF $\hat{q}_0(\boldsymbol{x})$ and $f(t)$.

```
if ||∂L/∂g_ξ||_2 < ϵ_spa and ||∂L/∂f||_2 < ϵ_tem then
    for n = 0, 1, ··· do
    solve compressible N–S (2.8) in time-advance from t = t_0 to t = t_f to
    obtain q'^(n)(t = t_f).
    determine λ(t_f) using (2.18).
    solve adjoint N–S (2.20) in time-inverse from t = t_f to t = t_0 using q̂^n
    and f^n(t) to obtain λ(t_0).
    determine μ^(n) to satisfy the constraint condition E[g(x); Q(t_0, x)] = δ_0^2.
    update spatial distribution q̂^(n+1) using (2.19).
    determine χ^(n) to satisfy the constraint condition ||f||_2 = 1.
    update f(t)^(n+1) using (2.21).
    end for
end if
```

$$\frac{\partial \mathcal{L}}{\partial f(t)} = 0 \Rightarrow -2\chi f(t) + \langle \boldsymbol{\lambda}(t), \rho(t)\boldsymbol{g}(t)\rangle = 0. \tag{2.21}$$

Here, the dagger (†) denotes the adjoint of the linear operator. For the derivation of the compressible adjoint equations, we followed the formulation by Ohmichi & Yamada (2021). In the above equations, we omitted the explicit spatial variable $\boldsymbol{x}$ from the arguments of functions for brevity. By taking the first variation of $\mathcal{L}$ with respect to the Lagrange multipliers, we recover the constraint conditions in (2.8), (2.13) and (2.14).

To update the spatial and temporal distribution of the optimal forcing, the standard steepest ascent method (Pringle & Kerswell 2010; Cherubini & De Palma 2013) can be applied. Algorithm 1 outlines the optimization process for the NLOF analysis. In this approach, the step size is independently determined by adopting the approach by Pringle *et al.* (2012). The remaining Lagrange adjoint multipliers, μ and χ, are determined from the constraint conditions. The convergence tolerances for the residuals, ϵ_{spa}, ϵ_{tem}, will be discussed in § 3.1.

2.3. *Numerical methods*

2.3.1. *Flow condition*

In this study, we investigated two-dimensional flow around a NACA0012 airfoil in the high-subsonic, low-Reynolds-number regime. Following the study by Bouhadji & Braza (2003), we selected the conditions of $M = 0.75$ and $Re = 2.0 \times 10^4$. The angle of attack (AoA) was set to 2°, a condition where low-frequency oscillation is not observed.

2.3.2. *Computational domain and grid*

We present the computational domain and grid used for the NLOF analysis. We set the origin of the coordinates at the midpoint of the airfoil's chord line, and the chord length c was taken as the reference length. The computational domain was a circular region with a radius of $60c$, including a sponge layer at its outer edge, as will be detailed in § 2.3.3.

Figure 1 shows the numerical grid near the airfoil. We considered a rounded trailing edge with a radius $0.0015c$, following Wolf & Lele (2012). A body-fitted O-type computational grid was employed. This topology allows us to apply a simple method to define the normal vector, avoiding the singular point at the trailing edge. The grid was clustered near the

https://doi.org/10.1017/jfm.2026.11280 Published online by Cambridge University Press

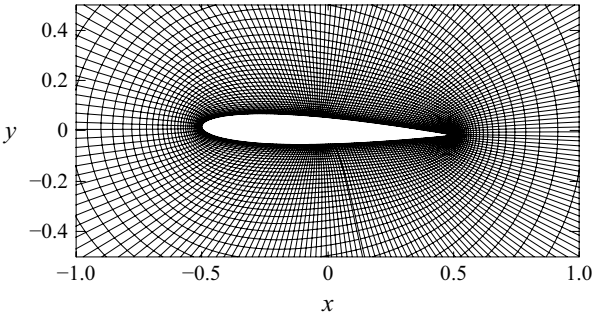


Figure 1. Computational grid in every five points near the airfoil at $AoA = 2°$.

airfoil surface to resolve the separated flow. The minimal grid spacing was 1.8×10^{-5} in the radial direction and 1.7×10^{-4} in the angular direction. The number of the grid points was 256 in the radial direction and 1024 in the angular direction.

2.3.3. *Numerical discretization method*

As discussed in § 2.2.4, we solve the compressible N–S equations and their adjoint counterparts. For the numerical discretization, Ohmichi & Yamada (2021) demonstrated that the compact finite difference method with appropriate boundary conditions yields highly accurate numerical results. Taniguchi *et al.* (2024*b*) subsequently applied this scheme to the nonlinear optimal perturbation method. In this study, we adopted the sixth-order compact difference method (Lele 1992) coupled with the tenth-order compact filtering method (Gaitonde & Visbal 2000). The free-parameter α_f of the compact filtering method, as described in (4) of Gaitonde & Visbal (2000), was fixed at $\alpha_f = 0.45$ for all computational conditions. Temporal discretization was performed using the third-order total variation diminishing Runge–Kutta method (Gottlieb & Shu 1998).

We imposed adiabatic wall conditions on the airfoil. For the far-field boundaries, we applied inflow conditions within the angular range of $\pm\pi/3$ (starting from the leading edge at an $AoA = 0°$) and outflow conditions for the remaining boundary. For the inflow, we utilized a non-reflecting inflow condition based on the Riemann-invariant approach (Mengaldo *et al.* 2014). For the outflow, we employed the local one-dimensional inviscid method proposed by Thompson (1987) and Poinsot & Lele (1992), adapted for curvilinear coordinates (Kim & Lee 2000). To suppress the reflection of acoustic waves at the far-field boundaries, we implemented sponge zones (Bodony 2006) at the edge of the computational domain, specifically within the annular region from an inner radius of $40c$ to an outer radius of $60c$.

2.3.4. *Numerical validation*

This section presents the numerical validation of our computational methods. Figure 2 compares the time-averaged lift coefficients at $M = 0.2$ with previous studies, specifically the experimental values from Ohtake *et al.* (2007) and two-dimensional laminar calculation results from Lee *et al.* (2017). At $Re = 10^4$, our calculated values agree well with both numerical and experimental data at low angles of attack, although they deviate from experimental values at high angles of attack. For the higher Reynolds number case, shown in figure 2(*b*), our current calculations also show good agreement with the numerical values reported by Lee *et al.* (2017), with the exception of a larger deviation at an $AoA = 3°$. In comparison, Kim, Chang & Chung (2011) reported $C_l = 0.40$ at $Re = 2.3 \times 10^4$ and $C_l = 0.49$ at $Re = 3.3 \times 10^4$ for a NACA0012 airfoil in a wind tunnel

https://doi.org/10.1017/jfm.2026.11280 Published online by Cambridge University Press

	Total grid points	$\bar{C}_l$	$\bar{C}_d$
Present	262 144	−0.08572	0.05183
Fine	409 600	−0.08573	0.05185

Table 1. Mesh dependency of time-averaged lift and drag coefficients at $M = 0.75$, $Re = 2 \times 10^4$, $AoA = 2°$.

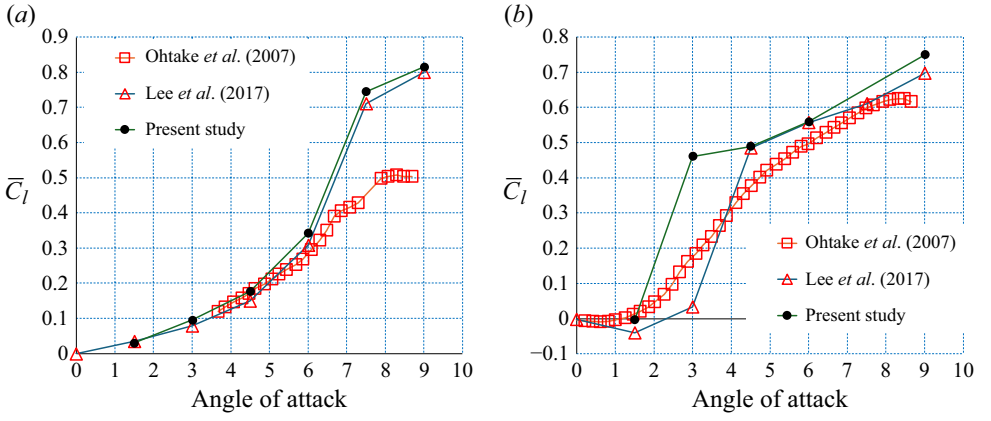


Figure 2. Variation of time-averaged lift coefficient with AoA at $M = 0.2$: (*a*) $Re = 10^4$; (*b*)$Re = 3 \times 10^4$.

experiment at this AoA. Our present calculated values fall within this expected range. Thus, we conclude that the current numerical scheme accurately captures the dependency of the lift coefficients on the AoA within the flow conditions considered in this study.

Second, we examine the mesh convergence of the calculation results. Table 1 presents the mesh dependency of the lift and drag coefficients. From this table, we conclude that the current numerical solutions is sufficiently converged with respect to the computational grid.

2.4. *Data analysis methods*

The application of optimal forcing induces spatiotemporal transient changes in the flow field. To analyse the unsteady behaviour of the flow changes, we adopted the variational mode decomposition-based non-stationary coherent structure (VMD-NCS) method proposed by Ohmichi (2024). The effectiveness of VMD-NCS has been previously demonstrated in revealing non-stationary fluid phenomena, for example, in the analysis of buffet cells (Ohmichi & Sugioka 2026).

Let $\boldsymbol{q}(t, \boldsymbol{x})$ represent flow data sampled at discrete time steps $t = t_1, t_2, \ldots, t_N$. First, we apply proper orthogonal decomposition (POD). We assume that the data can be projected onto an M-dimensional subspace spanned by POD basis vectors $\tilde{\boldsymbol{q}}_j(\boldsymbol{x})$ for $j = 1, 2, \ldots, M$. The flow field can then be represented as

$$\boldsymbol{q}(t, \boldsymbol{x}) = \sum_{j=1}^{M} a_j(t)\tilde{\boldsymbol{q}}_j(\boldsymbol{x}) \tag{2.22}$$

https://doi.org/10.1017/jfm.2026.11280 Published online by Cambridge University Press

where $a_j(t) = \langle \boldsymbol{q}(t, \boldsymbol{x}), \tilde{\boldsymbol{q}} \rangle$, and $\langle , \rangle$ denotes the inner product. Following Hanifi *et al.* (1996), we define the inner product for compressible flow fields as

$$\langle \boldsymbol{q}_1, \boldsymbol{q}_2 \rangle = \frac{1}{2} \int_{\Omega} \frac{\bar{\Theta} \rho_1 \rho_2}{\gamma \bar{\rho} M^2} + \bar{\rho}(u_{x1} u_{x2} + u_{y1} u_{y2}) + \frac{\bar{\rho} \Theta_1 \Theta_2}{\gamma \tilde{\gamma} \bar{\Theta} M^2} \mathrm{d}V, \tag{2.23}$$

where $\boldsymbol{q}_1, \boldsymbol{q}_2$ are arbitrary state vectors of the flow field. Consequently, the flow data can be entirely reconstructed as a point $\boldsymbol{a}(t) = (a_1(t), a_2(t), \ldots, a_M(t))^T$ in the POD basis coordinate system.

The core idea of VMD-NCS (Ohmichi 2024) is to apply multivariate VMD (Rehman & Aftab 2019) to this M-dimensional time series data, extracting modes termed intrinsic coherent structures (ICS) after mapping them back to the physical space. We briefly introduce this concept, starting with VMD analysis, which is originally proposed in the context of signal analysis by Dragomiretskiy & Zosso (2013) as an alternative to empirical mode decomposition. In this analysis, the signal data is converted into an analytic signal via the Hilbert transform and decomposed into a limited number of VMD modes which possess local frequency bands around the centre frequency. The extension of VMD into multivariate signals was given by Rehman & Aftab (2019), based on the assumption that all the variables of the data possess common oscillation properties. For an application to fluid dynamics, the validity of this assumption was demonstrated by Ohmichi (2024).

The mathematical formulation of multivariate VMD (MVMD) is thereby given as follows. The decomposition of multivariate signal $\boldsymbol{a}(t) = (a_1(t), a_2(t), \ldots, a_M(t))^T$ into K band-limited MVMD modes $\{(v^{k,1}(t), v^{k,2}, \ldots, v^{k,M})^T\}_k$ is formulated as an inverse problem to recover the signal as a linear combination of MVMD modes. Introducing Tikhonov regularization, this is achieved by solving the optimization problem of the functional (equation (14) in Rehman & Aftab (2019))

$$\sum_{m=1}^{M} ||a_m(t) - \sum_{k=1}^{K} v^{k,m}(t)||_2^2 + \alpha \sum_{m=1}^{M} \sum_{k=1}^{K} ||\partial_t [v_+^{k,m}(t) \mathrm{e}^{-\mathrm{i}\omega_k t}]||_2^2, \tag{2.24}$$

where $v_+^{k,m}$ is the analytical signal of $v^{k,m}$ and ω_k is the centre frequency of the kth MVMD mode. Note that this regularization term enforces a narrow-band frequency distribution around the centre frequency ω_k for the kth MVMD mode, while their linear combination recovers the original signal.

The number of ICS modes, K, and the regularization parameter α are user-defined. In the actual implementation, alternating direction method of multipliers is employed; for details, refer to Rehman & Aftab (2019) and Ohmichi (2024). The kth ICS, $\boldsymbol{\phi}_k$ is then reconstructed using the POD basis as

$$\boldsymbol{\phi}_k(t, \boldsymbol{x}) = \sum_{m=1}^{M} v^{k,m}(t) \tilde{\boldsymbol{q}}_m(\boldsymbol{x}), \tag{2.25}$$

where ϕ_k represents the extracted kth ICS in the physical space. This ICS represents the spatiotemporal structure within a narrow temporal frequency band around the centre frequency ω_k.

2.5. *Characteristic of the base flow field*

This section presents the characteristics of the base flow field at $M = 0.75$, $Re = 20\,000$, with an *AoA* of 2°. Figure 3 shows the power spectral density (PSD) of the lift coefficient

https://doi.org/10.1017/jfm.2026.11280 Published online by Cambridge University Press

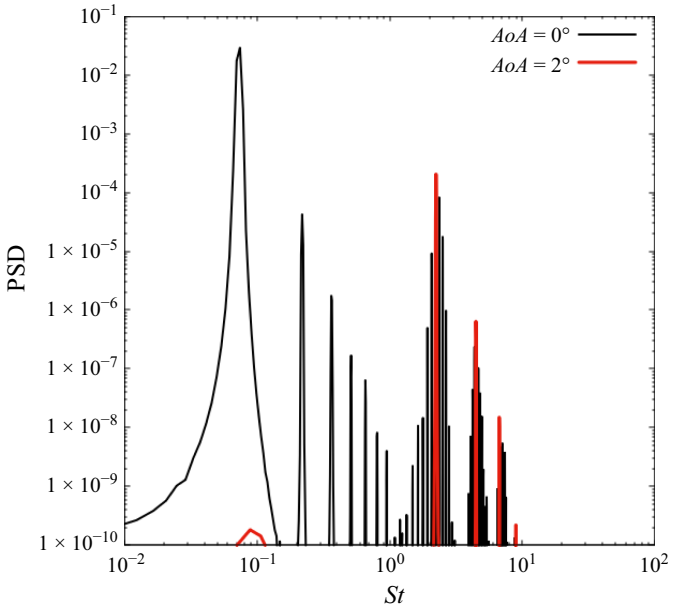


Figure 3. The PSD of lift coefficients of the base flow at $AoA = 0°$ and 2°.

of the base flow field, including a comparison with the $AoA = 0°$ case. In this analysis, we used the Hann window function to suppress spectral leakage. The (dimensionless) sampling period was 1.07×10^{-4} at $AoA = 0°$ and 1.12×10^{-4} at $AoA = 2°$. Data were obtained after sufficient time evolution from the initial condition.

In this figure, we observe that the flow field at $AoA = 0°$ exhibits a primary peak frequency at $St = 0.074$ and a secondary peak frequency at $St = 2.37$, where the first peak frequency shows a reasonable value compared with 0.06 at $Re = 10\,000$ in Bouhadji & Braza (2003) and 0.07 at $Re = 50\,000$ in three-dimensional calculations by Moise *et al.* (2024). Each peak frequency is accompanied by its integer multiples (harmonics). In contrast, the flow field at $AoA = 2°$ shows its primary peak frequency at $St = 2.24$. Although much weaker compared with the dominant frequency, a peak frequency at $St \approx 0.089$ is also present as a counterpart of the low-frequency oscillation at $AoA = 0°$. Therefore, the flow field at $AoA = 0°$ is characterized by two dominant peak frequencies, indicating a quasiperiodic behaviour where the low-frequency oscillation is a dominant phenomenon. In contrast, the flow field at $AoA = 2°$ exhibits a more periodic oscillation, with a negligible contribution from low-frequency oscillation.

Figure 4 presents the instantaneous flow field and time-history of the lift coefficient at $AoA = 2°$. This figure shows massive separation over the entire suction surface of the airfoil, accompanied by the shedding of von Kármán vortices in the wake. These features of the flow field show a qualitative agreement with the low-Reynolds number flow around a thick airfoil in smoke-wire visualizations reported by Kim *et al.* (2011). This vortex shedding is dominant, and a corresponding periodic variation in the lift coefficient is observed in figure 4(*b*). In this figure, the mean lift coefficient is negative, which is consistent with the negative lift slope characteristics in low Reynolds number flows around airfoils reported by Ohtake *et al.* (2007), Yonemoto *et al.* (2008) and Winslow *et al.* (2018).

https://doi.org/10.1017/jfm.2026.11280 Published online by Cambridge University Press

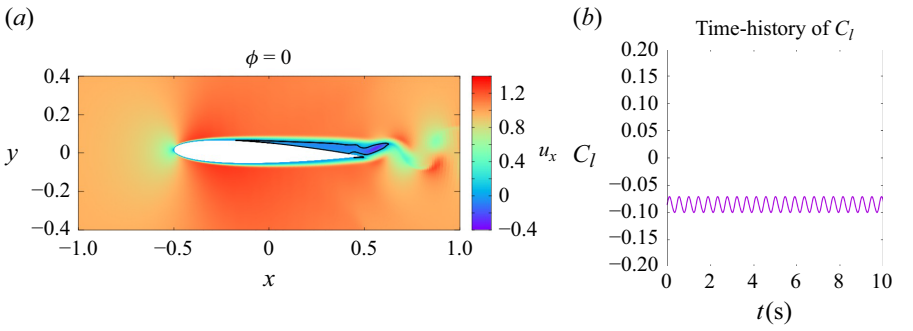


Figure 4. Instantaneous flow field at $\phi = 0$ and the time-history of C_l at $AoA = 2°$. The black curves in the instantaneous flow field represent the separation line zero-streamwise velocity isocontours ($u_x = 0$).

3. Extraction of NLOF

3.1. *Optimization of evaluation function*

We first examine the convergence of the solution obtained from the NLOF analysis solution. To evaluate the increase in entropy production, we define the percentage ratio of the evaluation function, $\mathcal{F}(t_f)$, as

$$\mathcal{F}(t_f) \times 10^{-2} = \frac{\mathcal{G}[t_f, \boldsymbol{q}(t, \boldsymbol{x})]}{\mathcal{G}[t_f, \boldsymbol{Q}(t, \boldsymbol{x})]} - 1. \tag{3.1}$$

Figure 5 shows a typical history of the optimization process. In this figure, the variation in the optimization is defined as $|\mathcal{F}^{(n+1)}(t_f) - \mathcal{F}^{(n)}(t_f)|$ during the update from step n to $n + 1$. We also present the residuals of the optimization process regarding the temporal and spatial distributions. As shown in this figure, the evaluation function was gradually updated and increased towards its maximum value. In the early optimization process, the evaluation function values improved rapidly towards their maximum values. When the evaluation function value increased and its fluctuation fell below 0.01, the convergence rate of the optimization calculation significantly decreased. This reduction in the variation of the evaluation function was proportional to the residuals of the optimization process, whose values were also influenced by the selection of the evaluation time. We set $\epsilon_{spa} = 5 \times 10^{-3}$ and $\epsilon_{tem} = 10^{-5}$ as the convergence tolerances for the residuals, ensuring that the variation of the evaluation function is less than 0.01, a level at which no significant changes of the optimal forces were observed.

The convergence properties of the optimization process were also affected by the selection of the step size. Selecting different step sizes in the temporal and spatial directions suppresses numerical oscillations during the optimization calculations. However, we confirmed that if either step size rapidly approaches zero, the likelihood of becoming trapped in a local optimum increases. As demonstrated in figure 5(*b*), the residuals gradually decreased, but completely eliminating numerical oscillations remained difficult. The primary factor hindering convergence is phase shifts in the time domain, which, coupled with the update of the spatial distribution, impede the optimization process. However, since these temporal shifts do not affect the changes in the separation region examined in this study, further improving of convergence efficiency is left as a future challenge.

https://doi.org/10.1017/jfm.2026.11280 Published online by Cambridge University Press

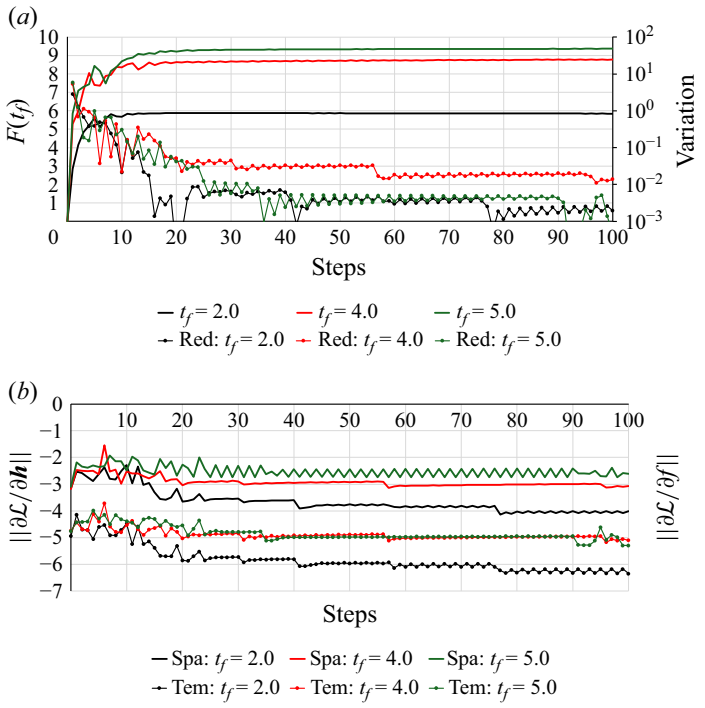


Figure 5. History of the evaluation function in the optimization process at $t_f = 2.0$, $\delta = 0.01$, $\phi = -\pi$. (*a*) Evaluation function value and its variation during the optimization. (*b*) Residuals for spatial and temporal distributions (semi-log plot).

3.2. *Characteristic of optimal forcing*

In this section, we investigate the spatiotemporal characteristics of the optimal forcing. For the following discussion, we introduce the growth rate of the disturbance field, defined as

$$G(t_f) = \frac{1}{\delta_0^2}\int_\Omega \frac{1}{2\bar{\rho}} m_i' m_i' \Big|_{t=t_f} \mathrm{d}V. \tag{3.2}$$

Figure 6 shows the spatial and temporal distributions of the optimal forcing for different amplitudes. The growth rate of the disturbance field is found to be inversely related to the amplitude of the external forcing: $G = 2.4 \times 10^4 (\mathcal{F} = 1.78)$ at $\delta_0 = 0.001$ whereas $G = 78.7 (\mathcal{F} = 9.8)$ at $\delta_0 = 0.02$. This significant reduction in gain is attributed to the nonlinear saturation of the disturbance growth. Conversely, the entropy production increases with increasing δ_0. This is because the definition in (2.11) is based on the total flow field, irrespective of its decomposition into base and disturbance components. In figure 6(*a*), the optimal forcing exhibits a locally concentrated spatial distribution just upstream of the laminar separation bubble of the base flow. In this linear regime ($\delta_0 = 0.001$), the temporal distribution shows a periodic pattern. Thus, for the small δ_0 case, the application of optimal forcing exploits the amplification mechanism of the disturbance field over the separation bubble, as reported in De Pando, Schmid & Sipp (2017) and Thomareis & Papadakis (2018).

Increasing the amplitude of external forces significantly alters the spatiotemporal characteristics. Spatially, the forcing concentrates in two primary regions: near the leading edge and around the separation point of the base flow field. The balance of intensity

https://doi.org/10.1017/jfm.2026.11280 Published online by Cambridge University Press

t_f	$\phi=-\pi$	$\phi=-\pi/2$	$\phi=0$	$\phi=\pi/2$
1.0	2.7[0.97]	2.7[1.1]	2.7[1.2]	2.7[0.79]
2.0	5.9[316]	5.4[193]	5.8[226]	6.5[375]
4.0	8.8[428]	9.0[390]	9.4[473]	8.9[437]
5.0	9.4[426]	10.1[487]	9.3[343]	9.5[415]

Table 2. Calculated evaluation function value ($\mathcal{F}$) at $\delta_0=0.01$ for various phases of the base flow. Values in brackets indicate the disturbance growth rate.

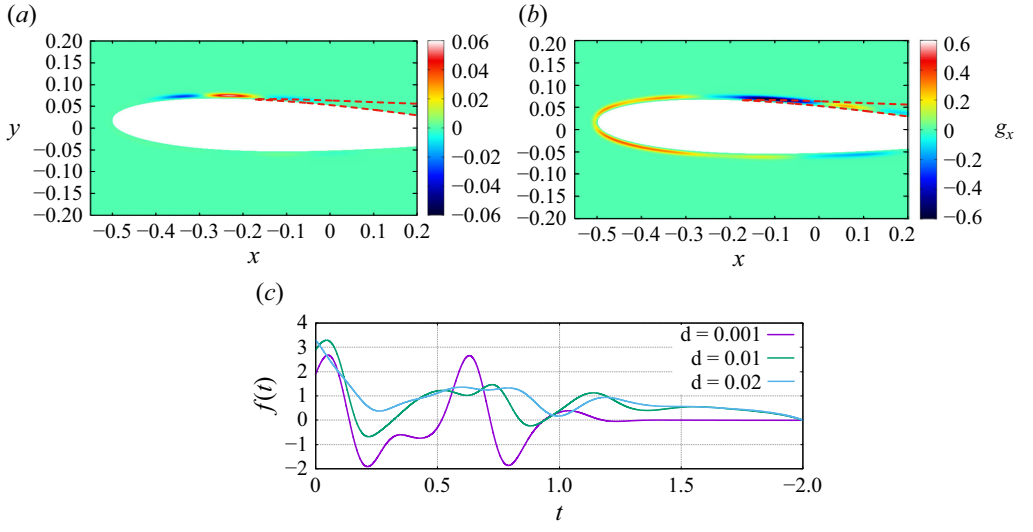


Figure 6. Spatial distributions of g_x at $t_f=2.0$, $\phi=-\pi$ for (a) $\delta_0=0.001$ and (b) $\delta_0=0.02$; (c) the temporal distributions at $AoA=2°$. The red dotted line indicates $\bar{u}_x=0$ contour of the base flow.

between these regions is governed by δ_0 and t_f. In the leading-edge region (especially for large δ_0 and small t_f), the forcing exhibits a streamwise-elongated spatial structure within the laminar boundary layer. This component is associated with a monotonically decreasing temporal profile, which serves to increase wall friction and generate high entropy production. Conversely, in the separation region, the forcing acts on the reverse flow. While this typically induces periodicity in linear regimes, high-amplitude forcing causes the perturbed flow to deviate significantly from the base flow, breaking the periodicity. Consequently, the temporal distribution in this region takes the form of a damped oscillation, reflecting the physical need for a strong initial impulse to shift the flow state. The superposition of these components results in a temporal distribution characterized by a damped oscillation with a positive mean value.

For $t_f>1.0$, the optimal forcing exhibits a non-uniform spatial distribution, with the temporal distribution dominated by a damped oscillation. Table 2 lists the calculated evaluation function values and disturbance growth rates. Notably, at larger evaluation times ($t_f=4.0$, 5.0), the disturbance growth rate exhibits a significantly stronger dependence on the phase of the base flow compared with the entropy production. This discrepancy implies that distinct flow trajectories can yield similar evaluation function values. Consequently,

https://doi.org/10.1017/jfm.2026.11280 Published online by Cambridge University Press

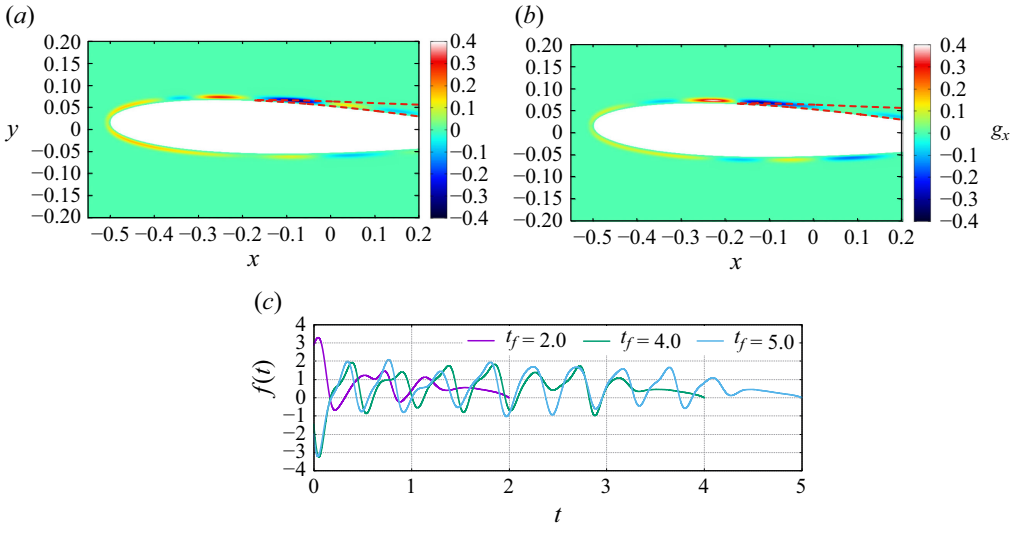


Figure 7. Spatial and temporal characteristics of the optimal forcing at $\phi = -\pi$, $\delta_0 = 0.01$, $AoA = 2°$: spatial distributions for (*a*) $t_f = 2.0$ and (*b*) $t_f = 5.0$; (*c*) temporal distributions t_f. The red dotted line indicates the $\bar{u}_x = 0$ contour of the base flow.

the presence of local optima within the current optimization framework cannot be ruled out.

For longer evaluation time (t_f), the periodic oscillation component in $f(t)$ becomes dominant; consequently, the time-averaged entropy production approaches a nearly constant value. As shown in table 2, the evaluation function value, averaged over the base flow phases, is $\mathcal{F} = 9.0$ at $t_f = 4.0$ and 9.5 at $t_f = 5.0$. This trend persists with further increases in evaluation time: for example, $\mathcal{F} = 9.4$ at $\phi = -\pi$, $t_f = 6.0$ and $\mathcal{F} = 9.6$ at $\phi = -\pi$, $t_f = 7.0$. This consistency suggests that the flow mechanisms induced by the optimal forcing remain qualitatively consistent as the evaluation time increases. Furthermore, the table indicates that the evaluation function is largely independent of the base flow phase. The unsteadiness at $AoA = 2°$ is primarily driven by von Kármán vortex shedding, whereas the spatial distribution of the optimal forcing is highly concentrated near the separation point of the base flow field. Given that the downstream vortex shedding exerts minimal influence on the upstream separation point, the observed independence of the control performance from the shedding phase is physically reasonable.

Figure 7 illustrates the spatial and temporal characteristics of the optimal forcing. Spatially, the forcing is primarily concentrated at the separation point of the base flow. We confirmed a high degree of similarity in the distributions across different t_f, with the exception that the upstream component near the leading edge gradually fades. This suggests that for longer t_f, the periodic forcing at the separation point becomes the dominant control mechanisms. Notably, for $t_f > 2.0$, the forcing patterns remain largely invariant.

To quantify the temporal characteristics, we analysed the frequency of $f(t)$ using VMD (Dragomiretskiy & Zosso 2013) combined with a Hanning window. Averaging the results from the eight cases ($t_f = 4.0$, 5.0) listed in table 2 yields a dominant frequency of $St = 2.11$ with a standard deviation of only 0.08. This low standard deviation demonstrates the robustness of the optimal forcing frequency, confirming its independence from the base flow phase and minor variations in evaluation time.

https://doi.org/10.1017/jfm.2026.11280 Published online by Cambridge University Press

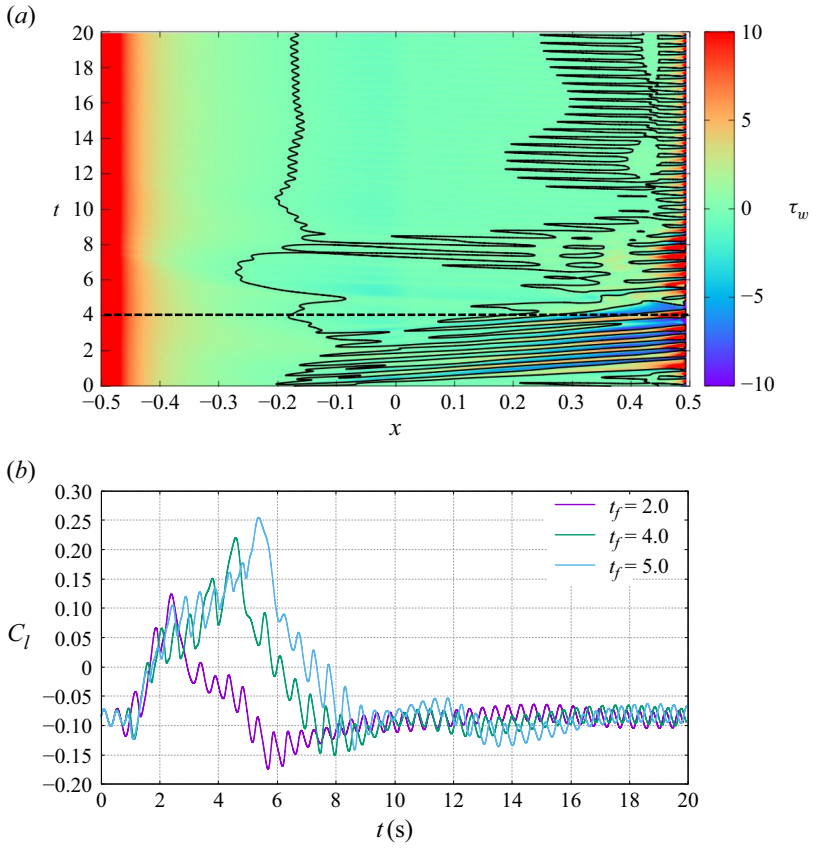


Figure 8. Changes in the flow field induced by the application of optimal forcing at $AoA = 2°$, $\phi = -\pi$ with an amplitude of $\delta_0 = 0.01$. The skin friction is shown for the case of $t_f = 4.0$, where the black curves represent the $\bar{u}_x = 0$ isocontours of the base flow, and the black dashed line indicates the evaluation time $t = t_f$. The forcing was applied from $t = 0$ to $t = t_f$. Here (*a*) skin friction; (*b*) lift coefficient.

3.3. *Changes of the flow field*

In this section, we examine the changes in the flow field induced by the application of optimal forcing. The external forcing produced clockwise vortices, which intensified as they propagated downstream from the separation point by extracting the energy from the shear layer of the base flow. Figure 8 shows the characteristics of the perturbed flow field in terms of skin friction and lift coefficients. An increase in the evaluation function values correlates with the integral value of the square of the skin friction coefficient, as defined in (2.10). In figure 8(*a*), a significant increase in skin friction is observed in association with vortex advection; the vortex trails appear as lines with a positive slope (indicating downstream movement). Moreover, the momentum transfer induced by the vortex advection caused the separation region to contract. Consequently, the separation point, which had been oscillating between points -0.175 and -0.163 in the base flow field, shifted downstream. This corresponds to the downstream shift of the separation point trace during the forcing application shown in figure 8(*a*). The contraction of the separation region accelerated the flow, resulting in a pressure decrease on the suction surface and a subsequent increase in the lift coefficient, as shown in figure 8(*b*). In this figure, we observe that the lift coefficient increases continuously with t_f. This corresponds to the fact that the

https://doi.org/10.1017/jfm.2026.11280 Published online by Cambridge University Press

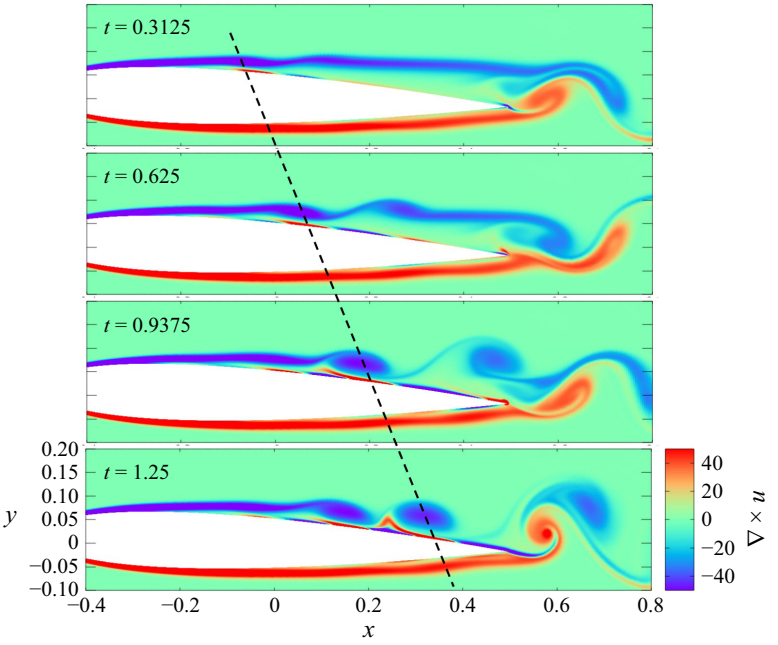


Figure 9. Spatial distribution of vorticity in the instantaneous flow field at $AoA = 2°$, $\phi = -\pi$. The optimal forcing was calculated for $t_f = 5.0$, $\delta_0 = 0.01$.

temporal distribution of the optimal forcing exhibits sustained periodicity for long t_f, as shown in figure 7(*c*). Therefore, we conclude that the lift increase is directly driven by vortex convection and can be sustained by the periodic passage of vortices through the separation region. This mechanism will be further investigated in the next section. As shown in figure 8(*a*), we also observe that the transient changes to the flow field persist even after the external forcing is removed, which will be discussed in § 3.4.

Figure 9 illustrates the physical process of vortex formation and convection along the airfoil. In this figure, the external forcing applied at the separation point of the base flow produces clockwise-rotating vortices that convect downstream. These vortices evolve by extracting energy from the shear layer between the free stream and the separated flow region. This process is analogous to the Kelvin–Helmholtz instability in inviscid flow. Concurrently with this vortex evolution in the shear layer, strong vorticity formation near the wall is observed due to the interaction between the shear layer and the wall surface. This eventually leads to the generation of secondary vortices (see $t_f = 1.25$ in the same figure), resulting in a local increase in skin friction. This vortex shedding process shows a qualitative similarity to the results of resolvent analysis over a separation bubble, as reported by Ricciardi, Wolf & Taira (2022). However, the present results demonstrate the emission of vortices with constant convective speed, as evidenced by the vortices trails in figure 8(*a*), which prevents complexities such as vortex pairing. This stable emission of vortices was consistently observed in the present simulations across multiple evaluation times.

3.4. *Transient changes of the flow field*

Next, we investigate the characteristics of the flow field changes driven by the advection of vortices induced by the optimal forcing. As shown in figure 8(*a*), this flow response exhibits a low-frequency oscillation that persists as transient dynamics even after the

https://doi.org/10.1017/jfm.2026.11280 Published online by Cambridge University Press

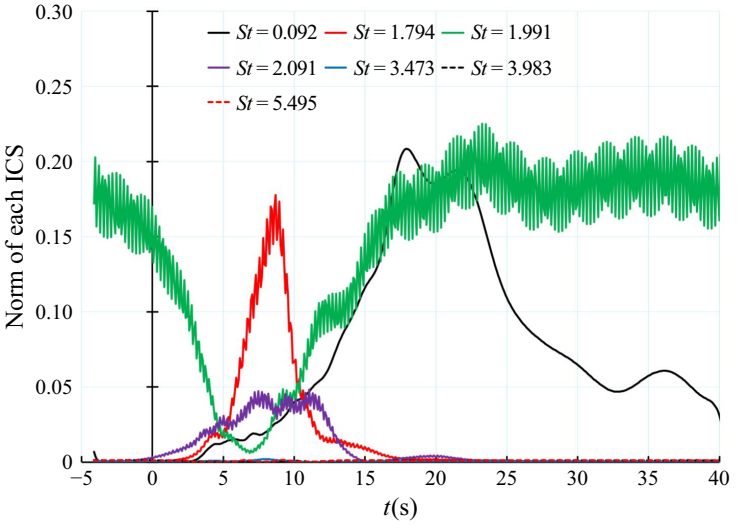


Figure 10. Time evolution of the norm of each ICS in the flow field perturbed by optimal forcing ($t_f = 2.0$, $\delta_0 = 0.01$). The forcing is activated during the interval $t = 0$ to $t = 2.0$.

forcing is removed. Since this behaviour shares characteristics with transonic buffet in high-subsonic flows, analysing these transient dynamics can shed light on the underlying oscillation mechanisms. In the remainder of this section, we present the results of VMD-NCS analysis for the case of $t_f = 2.0$. The flow evolution was computed from $t = -4.12$ to 40.4, with optimal forcing applied during the interval $0 \leqslant t \leqslant 2.0$. We extracted 512 snapshots at a sampling interval of $\Delta t = 0.087$. The VMD-NCS parameters were set to $K = 7$ and $\alpha = 5000$. The dependence of the analysis results on these parameters is examined in Appendix.

Figure 10 shows the time history of the magnitude of each ICS during its evolution, based on the definition in (2.23). In this figure, the dominant ICS at $St = 1.991$ is closely related to the primary peak frequency at $St = 2.24$ of the base flow field (figure 3), exhibiting a slight frequency shift under transient conditions. This dominant ICS at $St = 1.991$ exhibits a temporal decrease in magnitude between $0.0 \leqslant t \leqslant 25.0$, accompanied by the evolution of intermediate modes in the flow field. During this transient decay, two adjacent ICS at $St = 1.794$ and $St = 2.091$ emerge, governing the subsequent flow changes. As shown in figure 11 at $t = 8.08$, both of these ICS are characterized by the convection of vortices through the massive separation region on the suction surface. This observation strongly supports that the hypothesis that the breathing mechanism of the separation bubble is primarily driven by the momentum transfer associated with these convecting vortices.

Following the development of these transient modes, the magnitude of the ICS at $St = 0.092$ increases significantly. The frequency of this mode corresponds to the low-frequency oscillation of the base flow field in figure 3, and it also corresponds to the low-frequency oscillation observed after the removal of external forcing, as shown in figure 8(*a*). This low-frequency oscillation induced by external forces persists for a much longer duration ($t \leqslant 30$) than the original excitation period $0 \leqslant t \leqslant 2$. Recently, the connection of this low-frequency oscillation and transonic buffet is suggested by Moise *et al.* (2024), and clarifying the self-sustaining mechanism of this low-frequency oscillation may be critical to shed light the mechanism of low-frequency oscillations and hence the transonic buffet.

https://doi.org/10.1017/jfm.2026.11280 Published online by Cambridge University Press

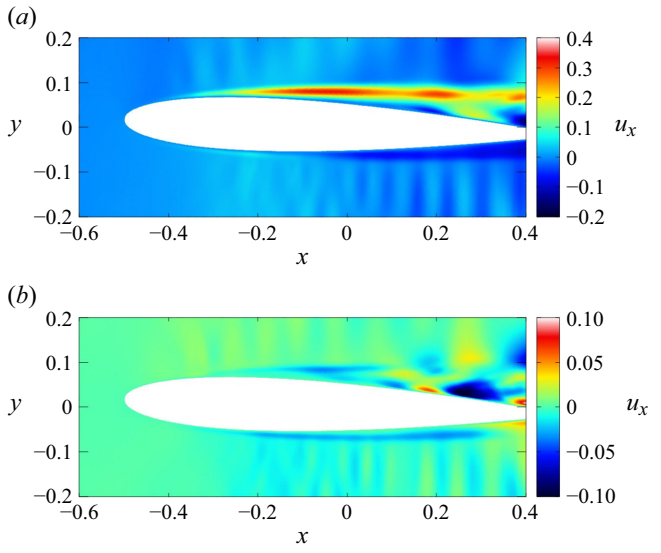


Figure 11. Instantaneous distribution of u_x in ICS at $t = 8.08$: (*a*) $St = 1.794$; (*b*) $St = 2.091$.

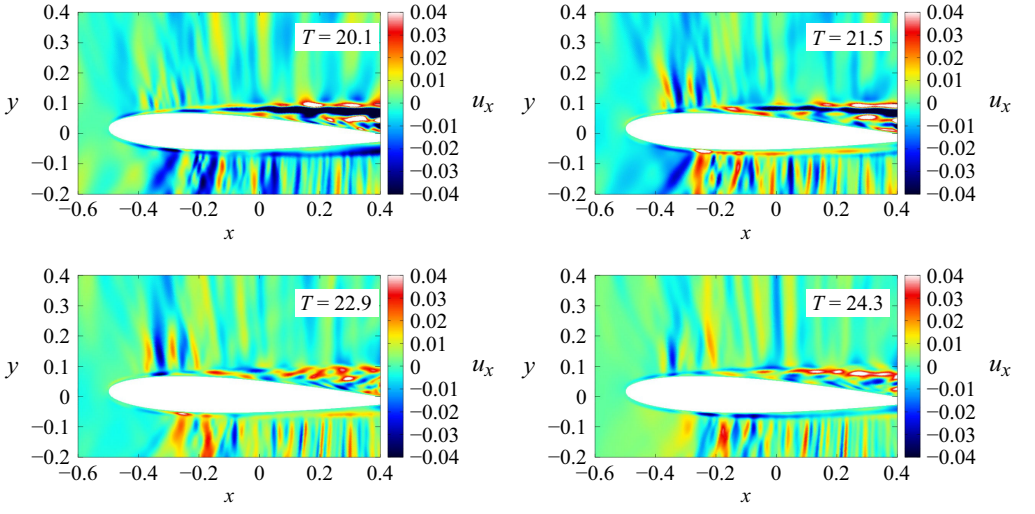


Figure 12. Spatiotemporal evolution of the ICS mode at $St = 0.092$, visualized over a half-period.

To explain the mechanism maintaining these low-frequency oscillations, a feedback loop mechanism similar to that observed in trailing-edge vortex noise (Desquesnes, Terracol & Sagaut 2007; Ricciardi *et al.* 2022) may be applicable. Figure 12 presents the instantaneous flow field of the ICS at $St = 0.092$. This figure visualizes a half-period of the flow field associated with the centre frequency of $St = 0.092$, showing the expansion and contraction of the separation region. The emission of acoustic waves from the trailing edge, accompanied by this low-frequency oscillation, is clearly observed; these waves interact with the airfoil surface, inducing velocity disturbances, particularly near the leading edge. At $T = 21.5$ and 22.9 in the same figure, velocity fluctuations are generated near the leading edge on the suction surface. These disturbances evolve into vortices that convect downstream, modulating the boundary layer state from deceleration to acceleration. As

https://doi.org/10.1017/jfm.2026.11280 Published online by Cambridge University Press

discussed regarding figure 8(*a*), the expansion and contraction of the separated boundary layer is attributed to momentum transfer caused by vortex convection along the airfoil. Therefore, for oscillations to be self-sustained, a mechanism that continuously supplies velocity fluctuations to the flow field is required. The velocity disturbances shown in figure 12 indicate that the interaction between acoustic waves and the boundary layer serves as this source.

The decay of the amplitude for the ICS at $St = 0.092$ after $t \geqslant 20$ indicates that the vortex generation induced by acoustic waves is insufficient to maintain the oscillation in the present flow field. Conversely, when the acoustic wave intensity is sufficiently high and the boundary layer is close to neutral stability, this low-frequency oscillation is expected to be sustained. Indeed, at a slightly higher Reynolds number of $Re = 5 \times 10^4$, the onset of the buffet phenomenon has been reported by Moise *et al.* (2024).

4. Application to impulsive flow control

4.1. *Simplification of temporal and spatial distribution for control application*

In this section, we examine the application of optimal forcing to suppress flow separation around an airfoil. As demonstrated in figure 8, applying external forcing over an appropriate time interval has the potential to increase the lift. This section focuses on using such external forcing to control the separated flow. Before implementing the control, however, the spatiotemporal distribution of the optimal forcing requires several simplifications to match the constraints of a realistic flow control system.

Based on the characteristics of the optimal forcing over long evaluation times (specifically $t_f = 4.0, 5.0$), we focus on forcing applied at the separation point of the base flow. The external forcing exhibits a concentrated distribution in the range $-0.35 \leqslant x \leqslant 0$ on the suction surface. We obtained a simplified spatial distribution by setting all values outside this range to zero and applying a cosine-tapered window function to ensure continuity at the domain boundaries. Specifically, the cosine-tapered function was treated as a one-dimensional function in the x-direction; it was set to unity within $[-0.35, 0]$ and included transition regions over $[-0.4, -0.35]$ and $[0, 0.1]$. This operation was applied only to the x-component, while the y-component was set to zero. The spatial profile was derived specifically from the spatial distribution of the optimal forcing at $\phi = -\pi$, $t_f = 5.0$, $\delta_0 = 0.01$, as shown in figure 7(*b*).

For the temporal distribution, we adopted a sinusoidal pattern with a frequency of $St = 2.11$, consistent with the results in § 3.2. We utilized a pulsed application of the optimal forcing with a repetition interval ΔT, defined as

$$\hat{f}(t) = \begin{cases} -A\sin(2\pi\omega s), & s \leqslant 1/\omega, \\ 0, & s > 1/\omega, \end{cases} \tag{4.1}$$

where A is the forcing amplitude, $\omega (= 2.11)$ is the forcing frequency, and the time is given by $t = m\Delta T + s$ with $m \in \mathrm{N}$ and $0 \leqslant s < \Delta T$.

Figure 13 shows the spatiotemporal distribution of the external forcing for the impulsive control of the flow field. Compared with the original distribution in figure 7(*b*), the present distribution eliminates low-amplitude regions while retaining the key structural features. Regarding the temporal statistics, the time-averaged power of the external force applied over one period ΔT can be calculated as

$$\mathcal{P}^2 = \frac{1}{\Delta T}\int_0^{\Delta T} |\hat{f}(t)|^2 \mathrm{d}t = \frac{A^2}{2\omega}\frac{1}{\Delta T}. \tag{4.2}$$

https://doi.org/10.1017/jfm.2026.11280 Published online by Cambridge University Press

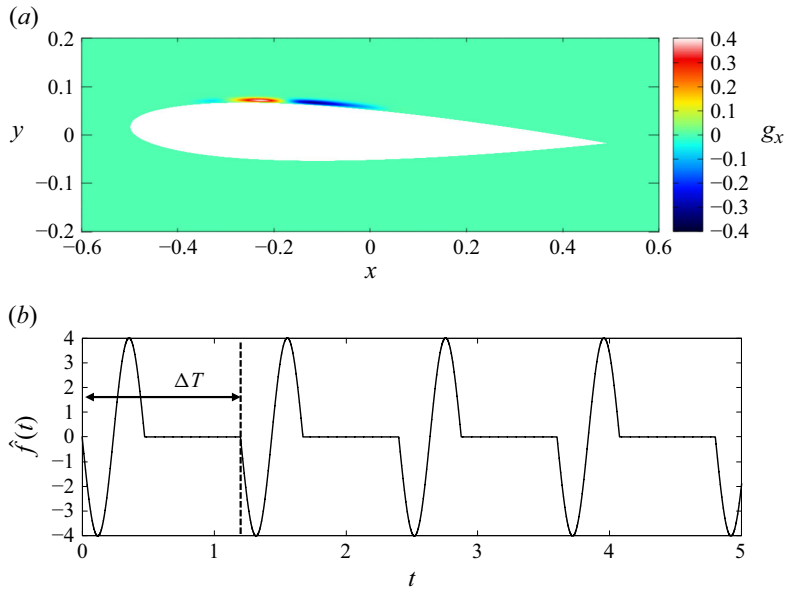


Figure 13. Spatiotemporal characteristics of the simplified external forcing used for impulsive flow control: (*a*) spatial distribution and (*b*) temporal distribution.

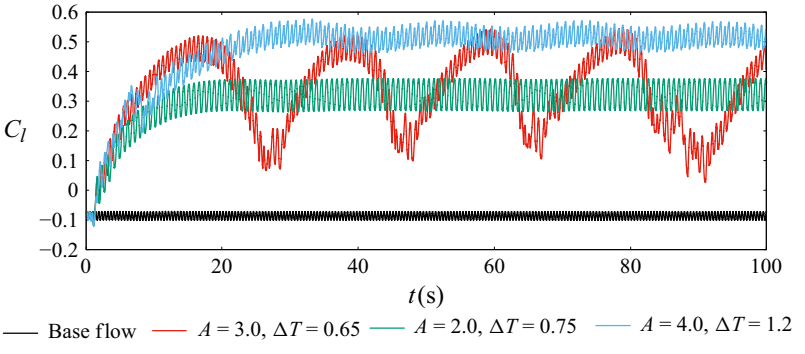


Figure 14. Time evolution of C_l during the impulsive application of external forcing.

This equation indicates that the power is inversely proportional to the pulse interval ΔT. Since the present optimal control analysis does not inherently determine the optimal pulse interval ΔT for long-term control, the appropriate interval will be determined through numerical experiments in the remainder of this section.

4.2. *Characteristics of forced flow field*

Figure 14 shows the time-evolution of C_l under the impulsive application of external forcing. In this figure, the C_l trajectory gradually deviates from the base flow and transitions into a new state sustained by the external force, exhibiting a significant increase in C_l compared with the base flow value (except for the case $A = 3.0$, $\Delta T = 0.65$). We found that the strong interactions between vortices caused flow unsteadiness when the pulse interval was short ($\Delta T < 0.75$). The intensity and pulse interval of the external force significantly affect the characteristics of the final flow field. Since the disturbance field

https://doi.org/10.1017/jfm.2026.11280 Published online by Cambridge University Press

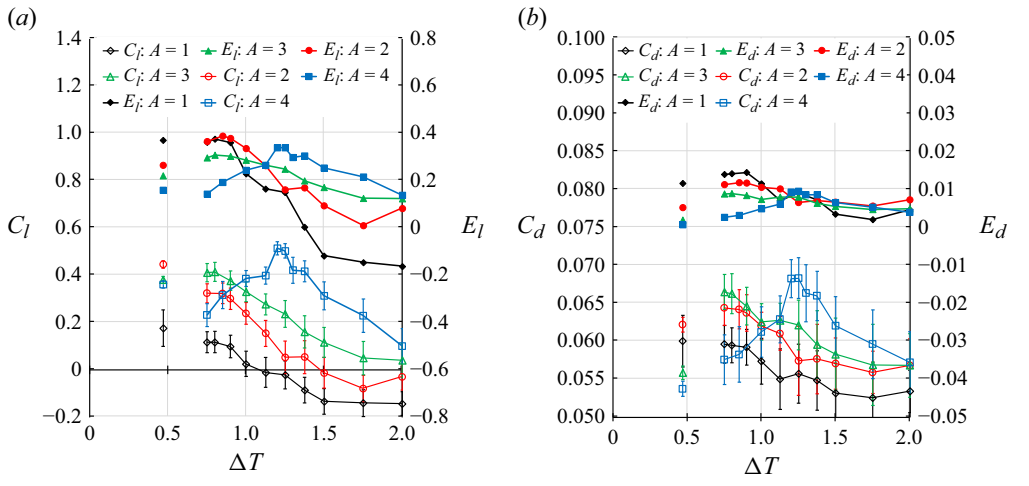


Figure 15. Converged aerodynamic coefficient under impulsive forcing: (*a*) time-averaged lift coefficient $\bar{C}_l$ and (*b*) drag coefficient $\bar{C}_d$. Error bars denote the standard deviation of the fluctuations.

cumulatively modifies the mean flow, we simulated the flow evolution for a sufficiently long duration ($t \geqslant 200$) to confirm the convergence of the flow statistics. In this figure, the early evolution of C_l exhibits similarities to the numerical results of separation control using plasma actuators reported by Asada *et al.* (2015) (see figure 6 therein). They noted that the impulsive actuation of a plasma actuator initially causes a decrease in the lift coefficient; this tendency was also observed in the present calculations.

Figure 15 presents the converged aerodynamic coefficients under impulsive forcing. We define the control efficiency $E_{l,d}$ as the gain in lift (drag) coefficient per unit input power, given by

$$E_{l,d} = \frac{\bar{C}_{l,d}[\boldsymbol{q}] - \bar{C}_{l,d}[\boldsymbol{Q}]}{\mathcal{P}}, \tag{4.3}$$

where $\bar{C}_{l,d}[\boldsymbol{q}]$ and $\bar{C}_{l,d}[\boldsymbol{Q}]$ represent the time-averaged lift (drag) coefficients for the forced ($\boldsymbol{q}$) and base ($\boldsymbol{Q}$) flows, respectively. A single pulse is applied per interval ΔT, with amplitude A and a spatial distribution based on figure 7. When the pulse interval is short ($\Delta T \leqslant 0.75$), close to the forcing period, complex vortex interactions prevent the flow from stabilizing. For larger intervals, the lift enhancement generally diminishes as ΔT increases. This occurs because the lift gain relies on vortex-induced momentum exchange, which scales with the pulse frequency ($1/\Delta T$). However, at high amplitudes, nonlinear vortex interactions alter this trend, producing a local maximum in lift at $\Delta T = 1.2$. Compared with the base flow values of $\bar{C}_l = -0.8572$ and $\bar{C}_d = 0.05183$ listed in table 1, the forced flow yields a higher lift coefficient than the base flow in all cases, except when the amplitude is low ($A = 1$) and the interval is long $\Delta T \geqslant 1.5$.

In terms of power efficiency (E_l), the optimal strategy depends on the pulse interval. At small intervals ($\Delta T = 0.75$), low-amplitude forcing is more efficient as it leverages the linear amplification of disturbances. At longer intervals ($\Delta T = 1.5$), however, high-amplitude forcing achieves better efficiency through nonlinear vortex interactions. Notably, the reduced frequency $F^+ = 1.25$ corresponding to the peak lift ($\Delta T = 1.2$, $A = 4$) agrees well with the value of $F^+ = 1.2$ reported for stalled airfoils at low Reynolds numbers by Greenblatt *et al.* (2008). This reduced frequency is defined as $F^+ =$

https://doi.org/10.1017/jfm.2026.11280 Published online by Cambridge University Press

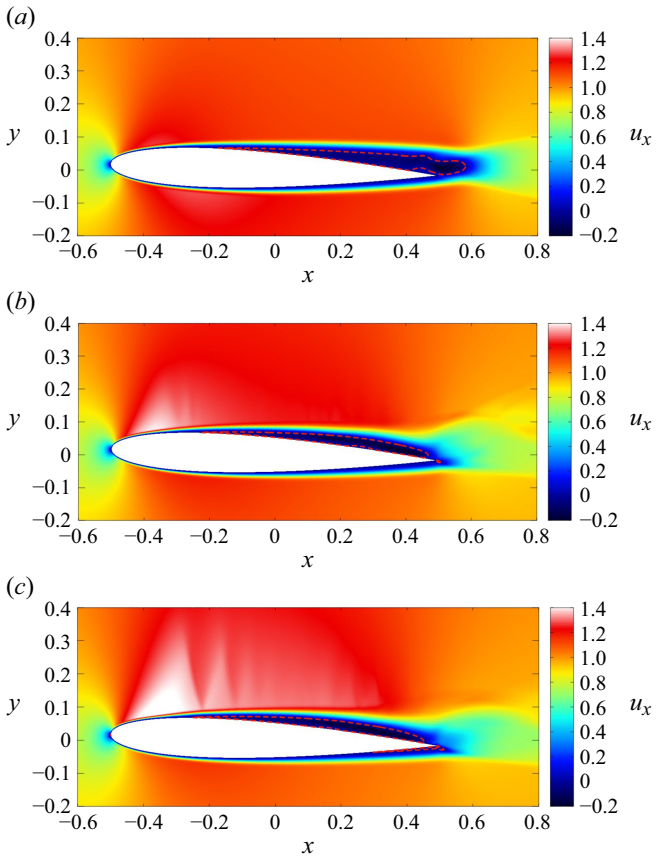


Figure 16. Spatial distribution of time-averaged streamwise velocity (u_x) for the base and forced flows. The red dashed line indicates the $u_x = 0$ contour: (*a*) base flow; (*b*) $A = 2.0$, $\Delta T = 0.75$; (*c*) $A = 4.0$, $\Delta T = 1.2$.

$X_{te}/(\Delta T U_\infty)$, where X_{te} is the distance from the forcing location to the trailing edge and U_∞ is the free stream velocity.

Next, we investigate the physical mechanism underlying the increase in C_l in the forced flow field. Figure 16 shows the spatial distribution of streamwise velocity for both the base flow and the forced flow. In the time-averaged base flow, a separation region extends beyond the trailing edge of the airfoil. This separation induces flow acceleration on the lower surface, which explains the negative lift observed in the base flow (Ohtake *et al.* 2007; Winslow *et al.* 2018). The application of external forcing facilitates momentum transfer between the vortices and the mean flow, leading to the reattachment of the separated flow on the upper surface, as shown in figures 16(*b*) and 16(*c*). This modification of the mean flow field causes acceleration on the upper surface, resulting in an increase in C_l due to the pressure difference between the upper and lower surfaces. We note that this acceleration region exhibits characteristics of shock waves, indicated by a local Mach number greater than unity. However, the generation of these shock waves does not induce significant changes in the flow field due to their weak intensity.

5. Conclusion

This study investigated optimal forcing to reattach separated flow around a NACA0012 airfoil at $M = 0.75$, $Re = 2.0 \times 10^4$ and its impulsive application for flow control. The

https://doi.org/10.1017/jfm.2026.11280 Published online by Cambridge University Press

characteristics of the optimal external forcing that maximize the evaluation function value differ depending on the evaluation time and its amplitude. It was found that the temporal distribution of the optimal forcing remained stable over long evaluation times, exhibiting a constant centre frequency. This frequency is interpreted as providing the minimum vortex interval required for stable emission into the separated flow region under a constant vortex amplitude. Indeed, when the vortex shedding spacing was reduced, the flow field became disordered due to destructive interference between the vortices. The increase of entropy production and the consequent rise in skin friction were attributed to the convection of vortices through the separation region.

The induced vortices amplified by extracting energy from the shear layer via the Kelvin–Helmholtz instability. However, nonlinear effects arising from finite-amplitude disturbances caused the shift in the spatial localization of the optimal forcing. This suggests that inducing acceleration and deceleration immediately downstream of the separation point is effective at high forcing intensities. Therefore, to generate strong vortices within a confined range, it is essential to apply an external force opposing the free stream to enhance shear and create clockwise-rotating vortices. The formulated analysis successfully elucidates the optimal forcing distribution to promote the reattachment of the separated flow via momentum exchange between vortices and shear layer. However, the generality of this conclusion for other flow fields, particularly those at high angles of attack, remains to be verified in future studies.

The present results indicate that the convection of vortices generated by the optimal forcing applied at the separation point causes a reduction in the separation region. Even after the external forcing is removed, velocity disturbances induced by acoustic waves temporarily sustain the low-frequency oscillations. This behaviour suggests that the wake mode, identified in the resolvent analysis of transonic buffet by Kojima *et al.* (2020), is the primary mechanism governing the expansion and contraction of the separation region, distinct from the higher-frequency buffet mode. To clarify this mechanism, further investigation focused on the transonic, low-Reynolds-number regime preceding buffet onset is required, particularly to elucidate the receptivity of the flow and the potential for triggering global instability via external forcing.

The investigation of impulsive flow control based on optimal external forcing yielded interesting results. The present findings indicate that, except when the external forcing amplitude is sufficiently high ($A = 4$), the continuous application of external forcing results in the greatest increase in the lift coefficient. These results seemingly contradict those from burst control studies, which suggest that intermittent external force application is more efficient for increasing lift (Greenblatt *et al.* 2008). Specifically, continuous forcing generates a dense, regular train of vortices that maximize the frequency of momentum transfer events, thereby maximizing the time-averaged lift. However, from the perspective of power efficiency, our findings align with previous conclusions; impulsive application creates sufficient lift enhancement while significantly reducing the required energy input. Furthermore, the consistent lift increase observed across varying external forcing intensities demonstrates the robustness of the flow control strategy derived in this study.

Acknowledgements. The authors thank the anonymous reviewers and the editor for their constructive comments and valuable suggestions, which helped improve this manuscript.

Funding. This study was supported by a Grant-in-Aid for JSPS Fellows (Grant No. 23KJ0831).

Declaration of interests. The authors report no conflict of interest.

https://doi.org/10.1017/jfm.2026.11280 Published online by Cambridge University Press

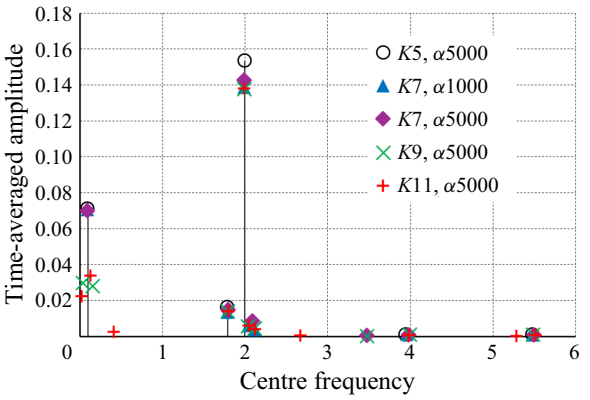


Figure 17. Influence of parameter K, α on the centre frequencies and its magnitude of the extracted ICS for the transient response analysis.

Appendix. Parameter setting in VMD-NCS analysis

In this Appendix, we examine the influence of the two user-defined parameters, K and α, on the VMD-NCS analysis. First, we present the parameter dependency observed in the transient response analysis from § 3.4. Figure 17 illustrates the observed centre frequencies and their time-averaged amplitudes after the application of forcing. Consistent with the description of Ohmichi (2024), we observed that as K increases, the spatiotemporal variations originally represented by a single ICS tend to be divided and expressed by multiple ICS. For example, the ICS with a centre frequency of $St = 0.092$ at $K = 7$, $\alpha = 5000$ was split into two separated ICS with centre frequencies of $St = 0.0405, 0.155$ when we set $K = 9$. However, this decomposition into a more detailed structure was not stabilized with a further increase in the total number of ICS (K) or with a change in α. When $K = 7$, significant dependency of the ICS selection on α was not observed, as shown by the amplitude changes with $\alpha = 1000$ and 5000. Therefore, we concluded that the setting of $K = 7$ is a suitable selection of the analysis, as it guarantees the robustness of the results.

References

Asada, K., Nonomura, T., Aono, H., Sato, M., Okada, K. & Fujii, K. 2015 LES of transient flows controlled by DBD plasma actuator over a stalled airfoil. *Intl J. Comput. Fluid D* **29** (3–5), 215–229.

Bodony, D.J. 2006 Analysis of sponge zones for computational fluid mechanics. *J. Comput. Phys.* **212** (2), 681–702.

Bouhadji, A. & Braza, M. 2003 Organised modes and shock–vortex interaction in unsteady viscous transonic flows around an aerofoil: Part I: Mach number effect. *Comput. Fluids* **32** (9), 1233–1260.

Butler, K.M. & Farrell, B.F. 1992 Three-dimensional optimal perturbations in viscous shear flow. *Phys. Fluids A: Fluid Dyn.* **4** (8), 1637–1650.

Cherubini, S. & De Palma, P. 2013 Nonlinear optimal perturbations in a Couette flow: bursting and transition. *J. Fluid Mech.* **716**, 251–279.

Cherubini, S., De Palma, P., Robinet, J.-C. & Bottaro, A. 2011 The minimal seed of turbulent transition in the boundary layer. *J. Fluid Mech.* **689**, 221–253.

Chu, S., Marensi, E. & Willis, A.P. 2025 Optimal body force for heat transfer in turbulent vertical heated pipe flow. *J. Fluid Mech.* **1019**, A21.

De Pando, M.F., Schmid, P.J. & Sipp, D. 2017 On the receptivity of aerofoil tonal noise: an adjoint analysis. *J. Fluid Mech.* **812**, 771–791.

Del Guercio, G., Cossu, C. & Pujals, G. 2014 Optimal streaks in the circular cylinder wake and suppression of the global instability. *J. Fluid Mech.* **752**, 572–588.

https://doi.org/10.1017/jfm.2026.11280 Published online by Cambridge University Press

DESQUESNES, G., TERRACOL, M. & SAGAUT, P. 2007 Numerical investigation of the tone noise mechanism over laminar airfoils. *J. Fluid Mech.* **591**, 155–182.
DRAGOMIRETSKIY, K. & ZOSSO, D. 2013 Variational mode decomposition. *IEEE Trans. Signal Process.* **62** (3), 531–544.
DUGUET, Y., MONOKROUSOS, A., BRANDT, L. & HENNINGSON, D.S. 2013 Minimal transition thresholds in plane Couette flow. *Phys. Fluids* **25** (8), 084103.
FARRELL, B.F. 1988 Optimal excitation of perturbations in viscous shear flow. *Phys. Fluids* **31** (8), 2093–2102.
GAITONDE, D.V. & VISBAL, M.R. 2000 Padé-type higher-order boundary filters for the Navier–Stokes equations. *AIAA J.* **38** (11), 2103–2112.
GIANNETTI, F. & LUCHINI, P. 2007 Structural sensitivity of the first instability of the cylinder wake. *J. Fluid Mech.* **581**, 167–197.
GOTTLIEB, S. & SHU, C.-W. 1998 Total variation diminishing Runge–Kutta schemes. *Maths Comput.* **67** (221), 73–85.
GREENBLATT, D., GOKSEL, B., RECHENBERG, I., SCHULE, C.Y., ROMANN, D. & PASCHEREIT, C.O. 2008 Dielectric barrier discharge flow control at very low flight Reynolds numbers. *AIAA J.* **46** (6), 1528–1541.
GREENBLATT, D. & WYGNANSKI, I.J. 2000 The control of flow separation by periodic excitation. *Prog. Aerosp. Sci.* **36** (7), 487–545.
GROSS, A., MARKS, C. & SONDERGAARD, R. 2024 Laminar separation control for Eppler 387 airfoil based on resolvent analysis. *AIAA J.* **62** (4), 1487–1502.
GUSTAVSSON, L.H. 1991 Energy growth of three-dimensional disturbances in plane Poiseuille flow. *J. Fluid Mech.* **224**, 241–260.
HANIFI, A., SCHMID, P.J. & HENNINGSON, D.S. 1996 Transient growth in compressible boundary layer flow. *Phys. Fluids* **8** (3), 826–837.
HUANG, Z. & HACK, M.J.P. 2020 A variational framework for computing nonlinear optimal disturbances in compressible flows. *J. Fluid Mech.* **894**, A5.
JONES, L.E., SANDBERG, R.D. & SANDHAM, N.D. 2006 Direct numerical simulation of the flow around an airfoil with unsteady wake. In *ECCOMAS CFD 2006: Proceedings of the European Conference on Computational Fluid Dynamics*. Citeseer.
JOVANOVIĆ, M.R. & BAMIEH, B. 2005 Componentwise energy amplification in channel flows. *J. Fluid Mech.* **534**, 145–183.
JUILLET, F., MCKEON, B.J. & SCHMID, P.J. 2014 Experimental control of natural perturbations in channel flow. *J. Fluid Mech.* **752**, 296–309.
JUKES, T.N., CHOI, K.-S., JOHNSON, G.A. & SCOTT, S.J. 2006 Characterization of surface plasma-induced wall flows through velocity and temperature measurements. *AIAA J.* **44** (4), 764–771.
KIM, D.-H., CHANG, J.-W. & CHUNG, J. 2011 Low-Reynolds-number effect on aerodynamic characteristics of a NACA 0012 airfoil. *J. Aircraft* **48** (4), 1212–1215.
KIM, J.W. & LEE, D.J. 2000 Generalized characteristic boundary conditions for computational aeroacoustics. *AIAA J.* **38** (11), 2040–2049.
KOJIMA, Y., YEH, C.-A., TAIRA, K. & KAMEDA, M. 2020 Resolvent analysis on the origin of two-dimensional transonic buffet. *J. Fluid Mech.* **885**, R1.
KONING, W.J.F., *et al.* 2024 Experimental results for mars rotorcraft airfoils (roamx-0201 and clf5605) at low Reynolds number and compressible flow in a Mars wind tunnel. NASA/TM-20240004230.
KOTSONIS, M. & VELDHUIS, L. 2010 Experimental study on dielectric barrier discharge actuators operating in pulse mode. *J. Appl. Phys.* **108** (11), 113304.
LAROUSSI, M., DJEBBI, M. & MOUSSA, M. 2014 Triggering vortex shedding for flow past circular cylinder by acting on initial conditions: a numerical study. *Comput. Fluids* **101**, 194–207.
LEE, D., NONOMURA, T., OYAMA, A. & FUJII, K. 2017 Comparative studies of numerical methods for evaluating aerodynamic characteristics of two-dimensional airfoil at low Reynolds numbers. *Intl J. Comput. Fluid Dyn.* **31** (1), 57–67.
LELE, S.K. 1992 Compact finite difference schemes with spectral-like resolution. *J. Comput. Phys.* **103** (1), 16–42.
LIM, J. & KIM, J. 2004 A singular value analysis of boundary layer control. *Phys. Fluids* **16** (6), 1980–1988.
LIU, Q., SUN, Y., YEH, C.-A., UKEILEY, L.S., CATTAFESTA III, L.N. & TAIRA, K. 2021 Unsteady control of supersonic turbulent cavity flow based on resolvent analysis. *J. Fluid Mech.* **925**, A5.
MAO, X., BLACKBURN, H.M. & SHERWIN, S.J. 2015 Nonlinear optimal suppression of vortex shedding from a circular cylinder. *J. Fluid Mech.* **775**, 241–265.
MARQUET, O., SIPP, D. & JACQUIN, L. 2008 Sensitivity analysis and passive control of cylinder flow. *J. Fluid Mech.* **615**, 221–252.

https://doi.org/10.1017/jfm.2026.11280 Published online by Cambridge University Press

MENGALDO, G., DE GRAZIA, D., WITHERDEN, F., FARRINGTON, A., VINCENT, P., SHERWIN, S. & PEIRO, J. 2014 A guide to the implementation of boundary conditions in compact high-order methods for compressible aerodynamics. In *7th AIAA Theoretical Fluid Mechanics Conference*, AIAA 2014-2923. American Institute of Aeronautics and Astronautics.

MOISE, P., ZAUNER, M. & SANDHAM, N.D. 2024 Connecting transonic buffet with incompressible low-frequency oscillations on aerofoils. *J. Fluid Mech.* **981**, A23.

MONOKROUSOS, A., ÅKERVIK, E., BRANDT, L. & HENNINGSON, D.S. 2010 Global three-dimensional optimal disturbances in the Blasius boundary-layer flow using time-steppers. *J. Fluid Mech.* **650**, 181–214.

MONOKROUSOS, A., BOTTARO, A., BRANDT, L., DI VITA, A. & HENNINGSON, D.S. 2011 Nonequilibrium thermodynamics and the optimal path to turbulence in shear flows. *Phys. Rev. Lett.* **106** (13), 134502.

NAGATA, T., NONOMURA, T., TAKAHASHI, S. & FUKUDA, K. 2020 Direct numerical simulation of subsonic, transonic and supersonic flow over an isolated sphere up to a Reynolds number of 1000. *J. Fluid Mech.* **904**, A36.

NATARAJAN, M., FREUND, J.B. & BODONY, D.J. 2016 Actuator selection and placement for localized feedback flow control. *J. Fluid Mech.* **809**, 775–792.

OHMICHI, Y. 2024 Variational mode decomposition–based nonstationary coherent structure analysis for spatiotemporal data. *Aerosp. Sci. Technol.* **149**, 109162.

OHMICHI, Y. & SUGIOKA, Y. 2026 Variational mode decomposition analysis of the relationship between low-frequency shock-wave oscillations and buffet cells. *Aerosp. Sci. Technol.* **168**, 110835.

OHMICHI, Y. & YAMADA, K. 2021 Matrix-free TriGlobal adjoint stability analysis of compressible Navier–Stokes equations. *J. Comput. Phys.* **437**, 110332.

OHTAKE, T., NAKAE, Y. & MOTOHASHI, T. 2007 Nonlinearity of the aerodynamic characteristics of NACA0012 aerofoil at low Reynolds numbers. *Japan Soc. Aeronaut. Space Sci.* **55** (644), 439–445.

POINSOT, T.J. & LELE, S.K. 1992 Boundary conditions for direct simulations of compressible viscous flows. *J. Comput. Phys.* **101** (1), 104–129.

POST, M.L. & CORKE, T.C. 2004 Separation control on high angle of attack airfoil using plasma actuators. *AIAA J.* **42** (11), 2177–2184.

PRALITS, J.O. & HANIFI, A. 2003 Optimization of steady suction for disturbance control on infinite swept wings. *Phys. Fluids* **15** (9), 2756–2772.

PRALITS, J.O., HANIFI, A. & HENNINGSON, D.S. 2002 Adjoint-based optimization of steady suction for disturbance control in incompressible flows. *J. Fluid Mech.* **467**, 129–161.

PRINGLE, C.C.T. & KERSWELL, R.R. 2010 Using nonlinear transient growth to construct the minimal seed for shear flow turbulence. *Phys. Rev. Lett.* **105** (15), 154502.

PRINGLE, C.C.T., WILLIS, A.P. & KERSWELL, R.R. 2012 Minimal seeds for shear flow turbulence: using nonlinear transient growth to touch the edge of chaos. *J. Fluid Mech.* **702**, 415–443.

REDDY, S.C. & HENNINGSON, D.S. 1993 Energy growth in viscous channel flows. *J. Fluid Mech.* **252**, 209–238.

REHMAN, N. & AFTAB, H. 2019 Multivariate variational mode decomposition. *IEEE Trans. Signal Process.* **67** (23), 6039–6052.

RICCIARDI, T.R., WOLF, W.R. & TAIRA, K. 2022 Transition, intermittency and phase interference effects in airfoil secondary tones and acoustic feedback loop. *J. Fluid Mech.* **937**, A23.

RIGAS, G., SIPP, D. & COLONIUS, T. 2021 Nonlinear input/output analysis: application to boundary layer transition. *J. Fluid Mech.* **911**, A15.

SCHMID, P.J. 2007 Nonmodal stability theory. *Annu. Rev. Fluid Mech.* **39** (1), 129–162.

SEKIMOTO, S., NONOMURA, T. & FUJII, K. 2017 Burst-mode frequency effects of dielectric barrier discharge plasma actuator for separation control. *AIAA J.* **55** (4), 1385–1392.

SUÁREZ, P., ALCÁNTARA-Á VILA, F., MIRÓ, A., RABAULT, J., FONT, B., LEHMKUHL, O. & VINUESA, R. 2025 Active flow control for drag reduction through multi-agent reinforcement learning on a turbulent cylinder at $Re_D = 3900$. *Flow Turbul. Combust.* **3900**, 1–25.

TAKAGAKI, M., ISONO, S., NAGAI, H. & ASAI, K. 2008 Evaluation of plasma actuator performance in Martian atmosphere for applications to Mars airplanes. In *4th Flow Control Conference*, AIAA 2008-3762. American Institute of Aeronautics and Astronautics.

TANIGUCHI, N., OHMICHI, Y. & SUZUKI, K. 2024*a* Entropy production-based nonlinear optimal perturbation for subsonic flows around an airfoil. *Phys. Fluids* **36** (9), 094115.

TANIGUCHI, N., OHMICHI, Y. & SUZUKI, K. 2024*b* Nonlinear transient disturbance growth analysis for the compressible external flow and application to a flow around circular cylinder. *J. Comput. Phys.* **516**, 113374.

THOMAREIS, N. & PAPADAKIS, G. 2018 Resolvent analysis of separated and attached flows around an airfoil at transitional Reynolds number. *Phys. Rev. Fluids* **3** (7), 073901.

https://doi.org/10.1017/jfm.2026.11280 Published online by Cambridge University Press

THOMPSON, K.W. 1987 Time dependent boundary conditions for hyperbolic systems. *J. Comput. Phys.* **68** (1), 1–24.

TREFETHEN, L.N., TREFETHEN, A.E., REDDY, S.C. & DRISCOLL, T.A. 1993 Hydrodynamic stability without eigenvalues. *Science* **261** (5121), 578–584.

VINUESA, R., LEHMKUHL, O., LOZANO-DURÁN, A. & RABAULT, J. 2022 Flow control in wings and discovery of novel approaches via deep reinforcement learning. *Fluids* **7** (2), 62.

WINSLOW, J., OTSUKA, H., GOVINDARAJAN, B. & CHOPRA, I. 2018 Basic understanding of airfoil characteristics at low Reynolds numbers (10^4-10^5). *J. Aircraft* **55** (3), 1050–1061.

WOLF, W.R. & LELE, S.K. 2012 Trailing-edge noise predictions using compressible large-eddy simulation and acoustic analogy. *AIAA J.* **50** (11), 2423–2434.

YEH, C.-A. & TAIRA, K. 2019 Resolvent-analysis-based design of airfoil separation control. *J. Fluid Mech.* **867**, 572–610.

YONEMOTO, K., TAKATO, K., OCHI, H. & FUJIE, S. 2008 Kutta condition violation in two-dimensional NACA0012 airfoil at low Reynolds number. In *26th AIAA Applied Aerodynamics Conference*, AIAA 2008-6399. American Institute of Aeronautics and Astronautics.

ZAMAN, K.B.M.Q. 1992 Effect of acoustic excitation on stalled flows over an airfoil. *AIAA J.* **30** (6), 1492–1499.

https://doi.org/10.1017/jfm.2026.11280 Published online by Cambridge University Press